Journal of Hepatocellular Carcinoma

Dovepress
Taylor & Francis Group

Open Access Full Text Article

ORIGINAL RESEARCH

Stromal ACTA2 Counteracts TCDD-Induced Hepatocarcinogenesis via Suppression of the PI3K–AKT–mTOR Pathway

Ruoyang He[1], Ziqing Yang[1], Wenge Zhang[1–3], Yuehao Ren[1], Shuzi Li[1], Simin Zhan[4], Chuntian Wang[5], Zhen Zhang[1]

[1]School and Hospital of Stomatology, Cheeloo College of Medicine, Shandong University, Shandong Key Laboratory of Oral Tissue Regeneration, Shandong Engineering Research Center of Dental Materials and Oral Tissue Regeneration, Shandong Provincial Clinical Research Center for Oral Diseases, Jinan, People's Republic of China; [2]Department of Rheumatology and Immunology, The First Affiliated Hospital, State Key Laboratory of Eye Health, School of Basic Medical Sciences, Division of Life Sciences and Medicine, University of Science and Technology of China, Hefei, People's Republic of China; [3]School of Biomedical Engineering, Suzhou Institute for Advanced Research, University of Science and Technology of China, Suzhou, People's Republic of China; [4]Department of Clinical Laboratory Medicine, The First Affiliated Hospital of Shandong First Medical University, Shandong Provincial Qianfoshan Hospital, Shandong Medicine and Health Key Laboratory of Laboratory Medicine, Jinan, People's Republic of China; [5]Department of Pediatric Surgery, The Second Qilu Hospital, Shandong University, Jinan, People's Republic of China

Correspondence: Zhen Zhang; Chuntian Wang, Email tg0170128@163.com; wangchuntianchina@126.com

Purpose: 2,3,7,8-Tetrachlorodibenzo-p-dioxin (TCDD) is a persistent environmental pollutant that promotes hepatocellular carcinoma (HCC) through non-genotoxic mechanisms. However, stromal regulatory factors that counteract its tumor-promoting effects remain poorly defined. This study aimed to elucidate the role of actin alpha-2 (ACTA2) in TCDD-associated hepatocarcinogenesis.

Methods: An integrative strategy combining network toxicology, Mendelian randomization, multi-omics and single-cell analyses, molecular docking and molecular dynamics simulations, along with in vitro experiments, was employed to investigate the functional role of ACTA2.

Results: ACTA2 was identified as a stromal-associated factor linked to reduced HCC risk and improved patient survival. Single-cell and multi-omics analyses revealed that ACTA2 is predominantly expressed in hepatic stellate cells and fibroblast-like populations, reflecting tumor microenvironment composition rather than tumor cell–intrinsic expression. Functional enrichment analyses indicated that ACTA2 is associated with extracellular matrix remodeling and PI3K–AKT signaling. Molecular simulations demonstrated stable binding of TCDD to ACTA2 ($\Delta G\_bind \approx -7.05$ kcal/mol), suggesting potential structural perturbation. In vitro experiments showed that TCDD downregulated ACTA2 expression, promoted proliferation of LX-2 and cancer-associated fibroblasts (CAFs), and activated PI3K–AKT–mTOR signaling, whereas ACTA2 overexpression attenuated these effects.

Conclusion: ACTA2 acts as a context-dependent stromal regulator that modulates PI3K–AKT–mTOR signaling in TCDD-induced hepatocarcinogenesis. These findings highlight the importance of stromal remodeling in environmental carcinogenesis and suggest ACTA2 as a potential biomarker and therapeutic target in dioxin-associated HCC.

Keywords: TCDD, ACTA2, PI3K–AKT–mTOR, hepatocellular carcinoma, environmental carcinogenesis

Introduction

2,3,7,8-Tetrachlorodibenzo-p-dioxin (TCDD) is a potent environmental contaminant belonging to the family of polychlorinated dibenzo-p-dioxins ("dioxins").[1–3] It is a persistent organic pollutant that accumulates in the food chain, human tissues, and the liver due to its lipophilicity and extremely slow elimination (half-life ~7–11 years).[4,5] Chronic exposure to TCDD has been linked to multiple cancers in animal studies. Notably, TCDD is considered a non-genotoxic carcinogen; it does not directly damage DNA, but instead promotes cancer through indirect mechanisms such as oxidative stress, chronic inflammation, and dysregulated cell signaling.[6,7]

https://doi.org/10.2147/JHC.S586916
Received: 5 December 2025
Accepted: 25 April 2026
Published: 10 May 2026

Liver hepatocellular carcinoma (LIHC) is among the most lethal malignancies worldwide, with a poor prognosis and limited treatment options.[8] Established LIHC risk factors include chronic hepatitis B/C infection, alcohol abuse, and non-alcoholic steatohepatitis, but growing evidence suggests that environmental toxicants like dioxins also contribute to liver carcinogenesis. Unlike potent genotoxins (eg. aflatoxin), TCDD is thought to act primarily as a tumor promoter – facilitating cancer development by altering the liver microenvironment and signaling networks rather than initiating mutations.[9] For example, long-term TCDD exposure in rodents leads to hepatic injury characterized by steatosis, inflammation, and fibrosis, pathological changes that often precede cirrhosis and LIHC.[10,11] This is consistent with TCDD's role as a high-affinity ligand of AhR, a transcription factor that controls xenobiotic responses and immune regulation. Aberrant AhR signaling due to dioxin binding can drive stellate cell activation and extracellular matrix deposition in the liver, thereby creating a pro-tumorigenic microenvironment. Indeed, experimental models have demonstrated that TCDD activates hepatic stellate cells (HSCs) via the Akt and NF-κB pathways, triggering the release of pro-inflammatory cytokines (TNF-α, IL-6) and promoting collagen deposition. Such an environment of chronic inflammation and fibrosis is highly conducive to hepatocarcinogenesis, as >90% of LIHC cases arise on a background of cirrhosis or advanced fibrosis.[12]

In recent years, significant advances have been made in the clinical management of HCC, particularly with the emergence of immunotherapy as a frontline systemic treatment for advanced-stage disease. Immune checkpoint inhibitors have demonstrated promising therapeutic efficacy, although their benefits remain heterogeneous and are influenced by tumor microenvironment characteristics and molecular heterogeneity. In addition, increasing evidence suggests that the identification of reliable prognostic biomarkers is essential for risk stratification and personalized treatment. For instance, several studies have reported that dysregulated expression of specific signaling molecules and cytoskeletal-related proteins is closely associated with tumor differentiation, recurrence, and patient survival outcomes. These findings highlight the complexity of HCC progression and underscore the need to further elucidate the molecular mechanisms linking environmental exposure, stromal remodeling, and tumor development.[13,14]

The PI3K–AKT–mTOR signaling pathway plays a central role in regulating cell growth, proliferation, and survival in liver cancer. Aberrant activation of this pathway is one of the most frequent molecular events in LIHC, occurring through genetic mutations, epigenetic alterations, or microenvironmental stimuli.[15] Once activated, PI3K catalyzes the generation of phosphatidylinositol-3,4,5-triphosphate (PIP_3), which recruits and activates AKT. Activated AKT subsequently phosphorylates multiple downstream substrates that suppress apoptosis, promote cell cycle progression, and enhance anabolic metabolism via mTOR signaling. Dysregulation of this axis contributes to uncontrolled hepatocyte proliferation, angiogenesis, and therapeutic resistance.[16] Importantly, environmental toxicants such as TCDD can perturb this signaling cascade through oxidative and inflammatory stress, indirectly activating PI3K–AKT–mTOR even in the absence of oncogenic mutations. Thus, chronic TCDD exposure may mimic tumorigenic signaling and facilitate malignant transformation by sustaining pro-survival and proliferative pathways in hepatocytes.[17] Emerging studies have further demonstrated that alterations in this pathway are not only associated with enhanced proliferative and invasive capacities of HCC cells but also closely linked to clinical prognosis. Experimental evidence indicates that modulation of key upstream regulators can significantly affect tumor growth, migration, and invasion through PI3K–AKT–mTOR signaling, as well as through crosstalk with other pathways such as Notch signaling. Moreover, recent bioinformatics and machine learning analyses have identified several critical genes involved in the transition from chronic liver disease to HCC, further emphasizing the central role of this signaling axis in disease progression and therapeutic targeting.[18,19]

Given the central role of fibrosis in hepatocarcinogenesis, ACTA2 (Actin Alpha 2, also known as α-smooth muscle actin, α-SMA) has emerged as a key marker of activated hepatic stellate cells and stromal remodeling.[20] ACTA2 encodes the primary actin isoform expressed in smooth muscle cells and myofibroblasts.[21] In the liver, it is minimally expressed under physiological conditions but becomes strongly upregulated in activated hepatic stellate cells (HSCs) and myofibroblasts during fibrogenesis.[22,23] ACTA2-positive myofibroblasts, which express α-SMA, are essential for extracellular matrix remodeling and wound repair and are characteristically abundant in fibrotic liver tissues.[24] In LIHC, ACTA2 expression primarily reflects the presence of fibrotic stroma derived from chronic liver injury rather than a tumor-intrinsic oncogenic process. Accumulating evidence suggests that fibrotic stroma not only reflects tissue damage but also actively participates in tumor initiation and progression by shaping the tumor microenvironment. Stromal components,

particularly cancer-associated fibroblasts derived from activated stellate cells, can modulate oncogenic signaling such as the PI3K–AKT–mTOR pathway through paracrine and structural mechanisms. Recent clinical studies have reported that higher ACTA2 levels in LIHC tissues are associated with longer patient survival, possibly because ACTA2 marks a fibrosis-rich but less aggressive tumor microenvironment. As the tumor progresses and malignant cells dominate, the proportion of fibroblasts declines, leading to reduced ACTA2 expression and poorer prognosis.[25] These findings suggest that ACTA2 may act as a context-dependent protective factor, maintaining stromal organization and restraining tumor progression.

In this study, we used a network toxicology approach to explore how TCDD contributes to LIHC development, focusing on the PI3K–AKT–mTOR pathway and its interaction with fibrogenic signaling. By integrating toxicogenomic datasets and LIHC transcriptomic profiles, we identified ACTA2 as a key hub gene linking TCDD exposure to hepatocarcinogenesis. Functional enrichment analysis highlighted the PI3K–AKT–mTOR signaling cascade as the principal pathway affected by TCDD. Cell-based experiments further demonstrated that TCDD downregulated ACTA2 while activating PIK3CA, AKT1, and mTOR, particularly at 48 hours post-exposure. Conversely, ACTA2 overexpression attenuated this activation, supporting its role as a stromal-associated regulator of PI3K–AKT–mTOR signaling. These results indicate that TCDD may promote hepatocarcinogenesis by reducing ACTA2 expression, thereby releasing the restraint on pro-survival and proliferative signaling. Collectively, our findings reveal a novel ACTA2–PI3K–AKT–mTOR regulatory axis, providing new mechanistic insight into how TCDD facilitates liver tumor development and highlighting ACTA2 as a potential protective biomarker and therapeutic modulator in toxin-associated LIHC.

Materials and Methods

Network Toxicology Analysis

Network Profiling of TCDD

The three-dimensional molecular structure of 2,3,7,8-tetrachlorodibenzo-p-dioxin (TCDD) was obtained from the PubChem database (https://pubchem.ncbi.nlm.nih.gov/). Toxicological features, including the predicted oral median lethal dose (LD_{50}) and key physicochemical descriptors, were calculated using the ProTox web server (https://tox.charite.de/). To systematically identify molecular targets potentially interacting with TCDD, target prediction data were integrated from three major repositories: the Comparative Toxicogenomics Database (CTD, https://ctdbase.org/), STITCH (http://stitch.embl.de),[26,27] and ChEMBL (https://www.ebi.ac.uk/chembl/).[28] The top 200 TCDD-associated genes from the CTD database were selected for further analysis to enhance biological specificity. All predicted targets were standardized, deduplicated, and merged to construct a comprehensive TCDD–target interaction network. This network provided the foundation for subsequent enrichment and causality analyses.

Druggable Mendelian Randomization Analysis

To elucidate potential causal associations between TCDD-related targets and LIHC, druggable candidate genes were retrieved from the Drug–Gene Interaction Database (DGIdb, version 4.2.0, https://www.dgidb.org/) and from the curated druggable gene list described by Finan et al Cis-protein quantitative trait loci (cis-pQTLs) from human peripheral blood were adopted as instrumental variables to examine the causal effects of protein expression on LIHC susceptibility. Protein QTL data were derived from the deCODE database, while GWAS summary statistics for LIHC were obtained from the FinnGen consortium (release R12). Mendelian randomization (MR) analyses were conducted using the TwoSampleMR R package (version 0.6.2). Independent single nucleotide polymorphisms ($r^2 < 0.001$) were retained to avoid linkage disequilibrium bias. The inverse variance weighted (IVW) approach served as the principal estimator, complemented by MR-Egger regression, MR-PRESSO, and leave-one-out sensitivity analyses to assess heterogeneity and horizontal pleiotropy. These procedures ensured the reliability and robustness of the inferred causal relationships between TCDD exposure–related proteins and LIHC risk.

Gene Expression Analysis of ACTA2

To comprehensively delineate the expression landscape and potential biological implications of ACTA2 in normal human tissues, we initially retrieved and analyzed transcriptomic data from the Human Protein Atlas (HPA, https://www.

proteinatlas.org/).[29–35] Using the tissue, single-cell, and subcellular modules of HPA, we evaluated the tissue-specific expression patterns, single-cell RNA sequencing (scRNA-seq) profiles, and immunofluorescence-based subcellular localization of ACTA2. Additionally, immunohistochemistry (IHC) staining images and HPA RNA-seq tissue sections of the liver were incorporated to validate and visualize its spatial expression pattern within hepatic tissue.

Subsequently, we employed the HUSCH database (http://husch.comp-genomics.org)[36] to present ACTA2 gene expression levels across reference cell types and further analyzed the HU 0205 Liver GSE136103 dataset to explore its single-cell distribution patterns and intercellular communication networks, highlighting its potential roles in hepatic microenvironmental regulation and cellular heterogeneity. To further elucidate the cell type–specific expression of ACTA2 in liver tissues, we accessed and integrated liver scRNA-seq datasets from the DISCO human single-cell omics database (https://www.immunesinglecell.org/),[37] refining cellular annotation and validating expression abundance across distinct cell lineages.

Moreover, to investigate the evolutionary conservation and functional stability of ACTA2 across vertebrate species, we conducted multiple sequence alignment and comparative conservation visualization using the UCSC Cancer Genomics Browser (https://genome-cancer.ucsc.edu/),[34] providing evolutionary evidence to support its biological significance.

Expression of ACTA2 in LIHC and Its Clinical Association

Importantly, given that ACTA2 is a canonical stromal marker, its expression in bulk transcriptomic datasets largely reflects stromal content (eg, fibroblasts and fibrosis) rather than tumor cell–intrinsic expression. Given the profound impact of gene expression on patients' clinical status, we conducted clinical correlation analyses using the TIMER2.0 database (http://timer.cistrome.org/),[38] the BEST database (https://rookieutopia.hiplot.com.cn/),[39] the scCancerExplorer database (https://bianlab.cn/scCancerExplorer/),[40] and the Kaplan-Meier Plotter database (https://kmplot.com/).[41,42]

Genetic Mutation Analysis of ACTA2

Using the cBioPortal platform (https://www.cbioportal.org/),[43–45] we performed a comprehensive analysis of ACTA2 gene alterations in LIHC based on the Combined Study dataset. Through the Cancer Types Summary module, we systematically examined the mutation spectrum and copy number alteration (CNA) frequency of ACTA2 across various TCGA tumor types. To further explore the association between ACTA2 genomic alterations and tumor immune characteristics, the TIMER3.0 database was employed to assess the correlation between ACTA2 CNAs and immune cell infiltration levels. In addition, leveraging the TISIDB platform (http://cis.hku.hk/TISIDB/), a curated resource for tumor–immune system interactions, we analyzed the co-expression patterns between ACTA2 and a wide range of immune-related genes, including immunomodulators, chemokines, and their corresponding receptors. Collectively, these integrative analyses provide valuable insights into the potential role of ACTA2 in shaping the tumor immune microenvironment.

ACTA2 Protein Mutation Site Analysis

We retrieved genetic mutation information of ACTA2 from 3046 patients (3095 samples) with hepatocellular carcinoma using the cBioPortal "Combined Study" dataset, which integrates multiple independent cohorts (TCGA, PanCancer Atlas; RIKEN, Nat Genet 2012; AMC, Hepatology 2014; MSK, PLOS One 2018; INSERM, Nat Genet 2015; MSK, JCO Precis Oncol 2023; MSK, Clin Cancer Res 2024; MSK, Clin Cancer Res 2018; MERiC/Basel, Nat Commun 2022; CLCA, Nature 2024), using the cBioPortal database (https://www.cbioportal.org/, Combined Study, accessed in March 2026).[43,44] The amino acid sequence of human ACTA2 was obtained from the UniProt database (https://www.uniprot.org/).[46] The complete wild-type and three mutant protein structures were predicted using AlphaFold3 (https://alphafoldserver.com/).[47] Subsequently, PyMOL software was used for three-dimensional visualization of the proteins, annotating protein domains and mutation sites. The "align" command was then used to compare the mutant proteins with the wild-type protein. This algorithm employs a dynamic exclusion strategy, iteratively optimizing over five rounds to progressively exclude poorly matched atoms, ultimately calculating the Cα atom root mean square deviation (RMSD) value. Finally, amino acid residues within 4 Å of the mutated residue were displayed, and residues forming hydrogen bonds with them were annotated.

Immune Infiltration Analysis

In this study, we comprehensively analyzed the association between ACTA2 expression and immune cell infiltration across diverse tumor types using publicly available databases, including TIMER3.0 (https://compbio.cn/timer3/) and TISIDB (http://cis.hku.hk/TISIDB/).[47,48] On the TIMER3.0 platform, partial correlation analyses were performed to evaluate the relationships between ACTA2 expression and the infiltration levels of major immune cell populations—such as B cells, T cells, natural killer (NK) cells, and dendritic cells—while controlling for tumor purity and considering various immune cell subsets and activation states. Subsequently, using the TISIDB database, we further examined the correlations between ACTA2 expression and multiple immune-related components of the tumor microenvironment, including lymphocyte infiltration, immunomodulatory molecules, chemokines, and their corresponding receptors. Collectively, these analyses elucidate the potential role of ACTA2 in orchestrating tumor–immune interactions and shaping the immune landscape across cancers.

Single-Cell Transcriptomic Analysis

To investigate the cell type–specific expression of ACTA2 within the tumor microenvironment of LIHC, we first retrieved single-cell RNA sequencing datasets related to LIHC from the TISCH2 database (http://tisch.compbio.cn/).[48,49] Three datasets with annotated fibroblast populations—GSE125449, GSE146409, and GSE166635—were selected for analysis. Based on the uniformly processed and annotated results provided by TISCH2, we obtained UMAP dimensionality reduction plots, ACTA2-overlaid UMAP feature plots, violin plots showing ACTA2 expression across cell types, cell–cell communication heatmaps, and outward signaling chord diagrams centered on key cell populations.

Subsequently, we accessed the GSE149614 LIHC dataset through the scCancerExplorer database (https://bianlab.cn/scCancerExplorer/) and obtained the integrated UMAP plot, ACTA2 expression distribution and violin plot, heatmaps of G1/S and G2/M cell cycle–related genes across cell types, and bar plots of cell-type proportions. UMAP plots were further recolored by cell type, tumor stage, sex, and sampling location to characterize the cellular composition and spatial distribution of the tumor microenvironment in the GSE149614 dataset.

Functional Enrichment Analysis

To investigate transcriptomic changes associated with ACTA2 expression in liver cancer, we analyzed in silico patient data. RNA-sequencing expression data for LIHC were obtained from The Cancer Genome Atlas (TCGA) via the UCSC Xena platform (https://xenabrowser.net). Clinical tumor samples (TCGA-LIHC) were stratified into ACTA2-high and ACTA2-low expression groups (using median ACTA2 expression as the cutoff). Differential expression analysis between these two groups was performed to identify genes correlated with ACTA2 levels.

Downstream enrichment analyses were then conducted to explore the biological pathways and processes associated with differential ACTA2 expression. Kyoto Encyclopedia of Genes and Genomes (KEGG) pathway enrichment and Gene Ontology (GO) term enrichment were carried out using the R package clusterProfiler. GO analysis encompassed the three GO domains: Biological Process (BP), Cellular Component (CC), and Molecular Function (MF). Additionally, gene set enrichment analysis (GSEA) was employed to validate and extend the enrichment findings, using the Hallmark, KEGG, and GO gene set databases for LIHC. Statistically significant enrichment was defined by an adjusted p value < 0.05. Data visualization, including dot plots for KEGG/GO over-representation and enrichment curves for GSEA, was performed in R to highlight the key pathways and processes associated with high versus low ACTA2 expression.

Molecular Dynamics Simulation

To evaluate the interaction between ACTA2 (actin alpha-2, smooth muscle) and 2,3,7,8-tetrachlorodibenzo-*p*-dioxin (TCDD), molecular docking and molecular dynamics (MD) simulations were performed. The three-dimensional structure of human ACTA2 was obtained from the SWISS-MODEL (P62736_5-377:8v2o.1.A). The structure of TCDD was retrieved from the PubChem database (https://pubchem.ncbi.nlm.nih.gov/) in SDF format and converted to PDBQT format using AutoDock Tools 1.5.7 (https://autodock.scripps.edu/). Protein preparation included removal of crystallographic water molecules, addition of polar hydrogens, and assignment of Kollman partial charges. Docking was

conducted to obtain a plausible ACTA2–TCDD binding pose, and the top-ranked binding orientation was used as the starting structure for simulation after removing any steric clashes. Protonation states for ionizable residues were assigned for pH 7.4 (with histidine tautomers chosen based on local hydrogen-bonding environments), and any missing side-chain atoms in the protein were built using standard modeling tools.

MD simulations of the ACTA2–TCDD complex were carried out using GROMACS 2022.4. The Amber14SB force field was applied for the protein, and General Amber Force Field (GAFF2) parameters for TCDD were generated with Antechamber (AmberTools), employing AM1-BCC charges for the ligand. Ligand parameters were converted to GROMACS format with ACPYPE. Each simulation system was solvated in a triclinic dodecahedral water box using the TIP4P water model, extending at least 1.2 nm from any solute atom. Neutralizing counterions (Na+/Cl−) were added to achieve a physiological salt concentration of 0.15 M using a Monte Carlo ion placement method. Periodic boundary conditions were imposed in all directions. Short-range electrostatic and van der Waals interactions were cut off at 1.0 nm (with the Verlet neighbor list scheme), and long-range electrostatics were computed with the Particle-Mesh Ewald (PME) method (real-space cutoff 1.0 nm, Fourier grid spacing ~0.12 nm, fourth-order interpolation). All covalent bonds involving hydrogen atoms were constrained using the LINCS algorithm (water geometry was constrained with SETTLE), permitting a 2 fs integration time step. The system temperature was maintained at 310 K using a velocity-rescale thermostat (T = 0.1 ps), and the pressure was maintained at 1 bar using a Parrinello–Rahman barostat (P = 2.0 ps; compressibility 4.5 × 10^−5 bar^−1). Center-of-mass motion was removed every 100 steps, and long-range dispersion corrections were applied for energy and pressure to account for cut-off truncation.

Prior to production MD, a multi-step equilibration protocol was employed: (1) energy minimization by steepest descent for up to 50,000 steps (converging at a force threshold of 1000 kJ·mol^−1·nm^−1); (2) a 100 ps constant-volume (NVT) equilibration at 310 K with positional restraints on the protein heavy atoms; and (3) a 100 ps constant-pressure (NPT) equilibration at 1 bar/310 K, gradually releasing the positional restraints. After equilibration, an unrestrained production MD run was conducted for 100 ns. Coordinates, velocities, and energies were recorded every 10 ps. Trajectory analyses were performed using built-in GROMACS tools to calculate the protein's root-mean-square deviation (RMSD) over time, per-residue root-mean-square fluctuation (RMSF), radius of gyration (R_g), solvent-accessible surface area (SASA), and the number of hydrogen bonds between ACTA2 and TCDD. The conformational free-energy landscape of ACTA2 (with and without TCDD) was mapped by projecting the 100 ns trajectories onto collective variables (eg, RMSD and R_g), and dominant conformational clusters were identified. Representative structures of the ACTA2–TCDD complex were extracted at 0, 25, 50, 75, and 100 ns for structural comparison and visualization of ligand positioning over time.

To estimate the binding affinity, the MD trajectories were subjected to MM/GBSA binding free energy calculations. Using the gmx_MMPBSA tool with the GBOBC2 implicit solvent model (igb = 5), snapshots from the last 20 ns of the production run (sampled every 100 ps) were analyzed to compute the average ΔGbind of TCDD to ACTA2 and its energetic components (van der Waals, electrostatic (Coulombic), polar solvation, and nonpolar solvation contributions).

Cell Experiments

Cell Culture

The human hepatic stellate cell line LX-2 (Procell, Wuhan, China) and human cancer-associated fibroblasts (CAFs; HyCyte, China) were used for in vitro functional assays. To enhance their activated phenotype, LX-2 cells were stimulated in vitro with recombinant human TGF-β1 (5 ng/mL; PeproTech, USA) for 24 h prior to subsequent experiments. Both LX-2 cells and CAFs were maintained in Dulbecco's Modified Eagle Medium (DMEM; Gibco, USA) supplemented with 10% fetal bovine serum (ExCell Bio, Uruguay) and 1% penicillin–streptomycin (Gibco, USA). Cells were cultured at 37 °C in a humidified atmosphere containing 5% CO_2. The culture medium was replenished every 2 days, and cells were subcultured at approximately 70–80% confluence. For treatments, cells were plated at the appropriate density and allowed to adhere overnight; LX-2 cells were then subjected to TGF-β1 activation as described above (if applicable), followed by exposure of both LX-2 cells and CAFs to TCDD (MedChemExpress, USA) at various concentrations (0, 0.1, 1, and 10 nM) for the indicated times, the 0.1–10 nM TCDD range was selected based on previous liver-related in vitro studies and on the bioaccumulative, highly lipophilic nature of TCDD, which makes nominal in vitro concentrations not directly comparable to circulating serum levels measured in exposed populations.[50]

Plasmid-Mediated ACTA2 Overexpression

To specifically overexpress ACTA2, LX-2 (ACTIVE) and CAF cells were transfected with an ACTA2 overexpression plasmid (Ov-ACTA2) or a non-targeting control plasmid (GenePharma, Shanghai, China). Transfections were performed using Lipofectamine 3000 (Invitrogen, USA) in Opti-MEM (Gibco, USA) following the manufacturer's protocol. Briefly, LX-2 (ACTIVE) and CAF cells were seeded in 6-well plates at approximately 30–40% confluency and transfected with plasmid at a final concentration of 50 nM. After 6 h, the transfection medium was replaced with fresh complete DMEM. For LX-2 (ACTIVE) cells, recombinant human TGF-β1 (5 ng/mL; PeproTech, USA) was added for 24 h to further enhance their activated phenotype, as described above, where applicable. Cells were then incubated for an additional 24–48 h to allow for ACTA2 overexpression before downstream TCDD treatment or functional assays. Overexpression efficiency was confirmed by quantitative real-time PCR (qRT-PCR) for ACTA2 mRNA and by Western blotting for ACTA2 protein, relative to β-actin as a loading control.

siRNA-Mediated ACTA2 Knockdown

To further investigate the functional role of ACTA2, loss-of-function experiments were performed using small interfering RNA (siRNA). LX-2 (ACTIVE) and CAF cells were transfected with ACTA2-specific siRNA (si-ACTA2) or negative control siRNA (NC) (GenePharma, Shanghai, China) using Lipofectamine 3000 (Invitrogen, Thermo Fisher Scientific, USA) in Opti-MEM (Gibco, Thermo Fisher Scientific, USA) according to the manufacturer's instructions. Briefly, cells were seeded in 6-well plates at approximately 30–40% confluency and transfected with siRNA at a final concentration of 50 nM. After 6 h, the transfection medium was replaced with fresh complete DMEM (Gibco, USA), and cells were further incubated for 24–48 h prior to downstream experiments. Knockdown efficiency was confirmed by Western blot analysis of ACTA2 protein levels, normalized to β-actin as a loading control.

Cell Proliferation Assay (CCK-8)

The effects of TCDD on LX-2 (ACTIVE) and CAF cell proliferation were assessed using the Cell Counting Kit-8 (CCK-8) colorimetric assay. Transfected or untransfected LX-2 (ACTIVE) and CAF cells were seeded into 96-well plates at an initial density of 5 × 10^3 cells per well and allowed to attach overnight. Cells were then treated with TCDD at 0, 0.1, 1, or 10 nM. At designated time points (0, 12, 24, 36, and 48 h post-treatment), 10 μL of CCK-8 reagent (Beyotime, China) was added to each well and incubated for 1 h at 37 °C. Absorbance at 450 nm was measured with a microplate reader (Thermo Fisher Scientific, USA) to determine cell viability. Each treatment condition and time point was assayed in six technical replicates, and each experiment was performed in triplicate (biological repeats).

Quantitative Real-Time PCR (qRT-PCR)

Treated LX-2 (ACTIVE) and CAF cells were harvested for gene expression analysis. Total RNA was extracted using Trizol reagent (Takara, Japan) according to the manufacturer's instructions. Purified RNA (1 μg) was reverse-transcribed into cDNA using the Evo M-MLV RT Mix Kit (Accurate Biology, China). qRT-PCR was carried out using a LightCycler 480 II system (Roche, Switzerland) with SYBR Green Premix Pro Taq HS qPCR Kit (Accurate Biology, China). Specific primer pairs were used to quantify ACTA2 and key PI3K/Akt pathway genes (PIK3CA, AKT1, and MTOR). Primer sequences were synthesized by General Biosystems (Anhui, China). The housekeeping gene β-actin was used as an internal control. PCR reactions were performed in triplicate for each sample. Relative mRNA expression levels were calculated by the 2^−ΔΔCt method, and results were normalized to the control group.

Statistical analysis was applied to compare experimental groups. Unless otherwise specified, data are presented as mean ± standard error of the mean (SEM) of at least three independent experiments. Group comparisons were made using one-way ANOVA followed by Tukey's post-hoc test or by Student's *t*-test, as appropriate. A threshold of $p < 0.05$ was considered statistically significant.

Western Blot Assay

To investigate the regulatory effect of ACTA2 on the PI3K–AKT–mTOR signaling pathway, including both gain- and loss-of-function conditions, we performed protein level analysis using Western blot technology. LX-2 (ACTIVE) and CAF cells subjected to ACTA2 overexpression or siRNA-mediated knockdown were used as cell models, and total protein was extracted

using RIPA lysis buffer (Beyotime, Shanghai, China). Protein concentration was determined using a BCA protein assay kit (Beyotime, Shanghai, China). Equal amounts of protein from each sample were loaded onto SDS-PAGE gels and transferred to PVDF membranes. After blocking, the membranes were incubated with primary antibodies overnight at 4°C. The primary antibodies used in this study were as follows: anti-ACTA2 (1:6000,14,395-1-AP, Proteintech Group, Inc, Wuhan, China), anti-PI3K (1:20,000, 60,225-1-Ig, Proteintech Group, Inc, Wuhan, China), anti-p-PI3K (1:400, AF3242, Proteintech Group, Affinity, Jiangsu, China,), anti-AKT (1:2000; 10,176-2-AP, Proteintech Group, Inc Wuhan, China), anti-p-AKT (Ser473) (1:3,000; 28,731-1-AP, Proteintech Group, Inc, Wuhan, China), anti-mTOR (1:4000,28,273-1-AP, Proteintech Group, Inc, Wuhan, China), anti-p-mTOR (1:10,000,67,778-1-Ig, Proteintech Group, Inc, Wuhan, China), anti-Beta-actin (1:1000, 66,009-1-Ig, Proteintech Group, Inc, Wuhan, China) After washing, these membranes were incubated with corresponding secondary antibodies The target protein bands on the membranes were detected using an ECL Western blot detection kit (Beyotime, Shanghai, China), and finally, the band grayscale values were quantitatively analyzed using ImageLab software.

Colony Formation Assay Using Conditioned Media

To evaluate the effects of stromal-derived factors on the clonogenic capacity of hepatocellular carcinoma (HCC) cells, colony formation assays were performed using conditioned media (CM). Human HCC cell lines Huh7 and Hep3B were seeded into 6-well plates at a density of 500–800 cells per well and allowed to adhere overnight.

Conditioned media were collected from LX-2 cells and cancer-associated fibroblasts (CAFs) after 48 h of culture, centrifuged to remove debris, and used to culture HCC cells. The medium was refreshed every 3 days. After 10–14 days of incubation, colonies were fixed with 4% paraformaldehyde and stained with 0.1% crystal violet.

Colonies containing more than 50 cells were counted under a microscope. Each experiment was performed in triplicate.

Results

Network Toxicology Analysis and Mendelian Randomization of TCDD

To investigate the potential molecular mechanisms underlying the association between TCDD exposure and LIHC a network toxicology and Mendelian randomization (MR) approach was employed. The three-dimensional structure of TCDD is presented in Figure 1A. Protox-based predictions indicated high toxicity, with an estimated LD_{50} of 1 mg/kg and a toxicity class of 1, suggesting strong toxic potential (Figures 1B and C). Disease enrichment results from the CTD database showed that TCDD was primarily linked to cancer, nervous system, and metabolic diseases (Figure 1D). Target prediction using the STITCH database identified multiple genes associated with cytochrome P450–related metabolic pathways (Figure 1E). MR analysis further revealed several candidate genes causally associated with LIHC risk, among which ACTA2 demonstrated significant correlation (Figure 1F). Integration of predicted targets from the ChEMBL, CTD, and STITCH databases yielded a total of 259 unique genes. Among them, the top 200 TCDD-associated genes retrieved from the CTD database were included to ensure biological relevance. Only a small overlap was observed among the three datasets, indicating that each database contributed distinct yet complementary information on TCDD-related targets (Figure 1G). Functional categorization showed that most targets were membrane receptors and enzymes (Figure 1H). Finally, Venn analysis identified ACTA2 as the sole overlapping gene between TCDD-related targets and LIHC-associated genes (Figure 1I), suggesting that ACTA2 may serve as a potential mediator linking TCDD exposure to hepatocarcinogenic processes.

Multi-Level Expression Profiling and Evolutionary Conservation of ACTA2

Based on transcriptomic and proteomic data from the Human Protein Atlas (HPA), DISCO, and HUSCH databases, we systematically characterized the multi-level expression and evolutionary features of ACTA2 across human tissues and cell types (Figures 2–4).

At the tissue level (Figures 2A and B), RNA expression profiling in HPA revealed that ACTA2 is highly expressed in smooth muscle–rich tissues, including the endometrium, seminal vesicles, and smooth muscle, whereas its overall expression in the liver is low, consistent with the relatively sparse presence of smooth muscle cells and myofibroblasts in normal hepatic architecture.

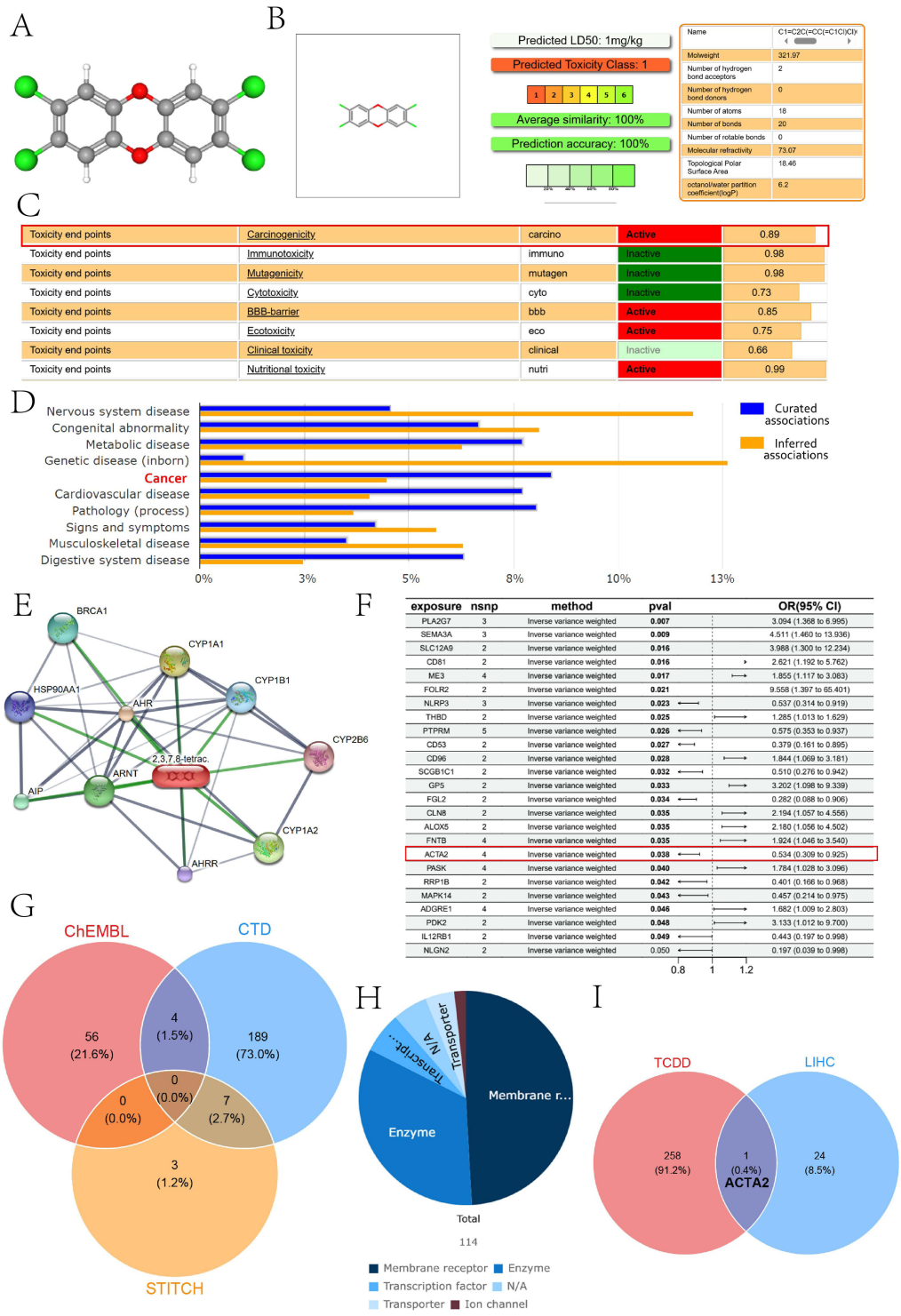

Figure 1 Network toxicology and Mendelian randomization analyses of TCDD. (**A**) The 3D molecular structure of TCDD. Carbon atoms are shown in gray, hydrogen atoms in white, oxygen atoms in red, and chlorine atoms in green. (**B** and **C**) Predicted toxicity profile of TCDD generated through the Protox online platform. In panel C, the red box highlights the predicted carcinogenicity endpoint (Active), indicating a potential carcinogenic risk. Different shades of green indicate the confidence level of the "Inactive" prediction, with darker green representing higher prediction probability. (**D**) Disease classifications linked to TCDD obtained from the Comparative Toxicogenomics Database (CTD). The category "Cancer" is highlighted in red to emphasize its relevance as the primary disease focus of this study. (**E**) Predicted TCDD target genes identified using the STITCH database. (**F**) Summary table of Mendelian randomization (MR) results highlighting the screened causal target. The red box indicates the key gene (ACTA2) identified as having a statistically significant causal association. Arrows indicate that the corresponding effect estimates or confidence intervals extend beyond the displayed range of the plot. (**G**) Venn diagram illustrating the overlap of predicted targets among the ChEMBL, CTD, and STITCH databases. (**H**) Potential molecular targets of TCDD predicted by the ChEMBL database. (**I**) Overlapping genes between TCDD-associated targets and liver hepatocellular carcinoma (LIHC)–related genes. The overlapping gene (ACTA2) is highlighted in the center, indicating its potential role as a key mediator.

https://doi.org/10.21147/JHCS586916

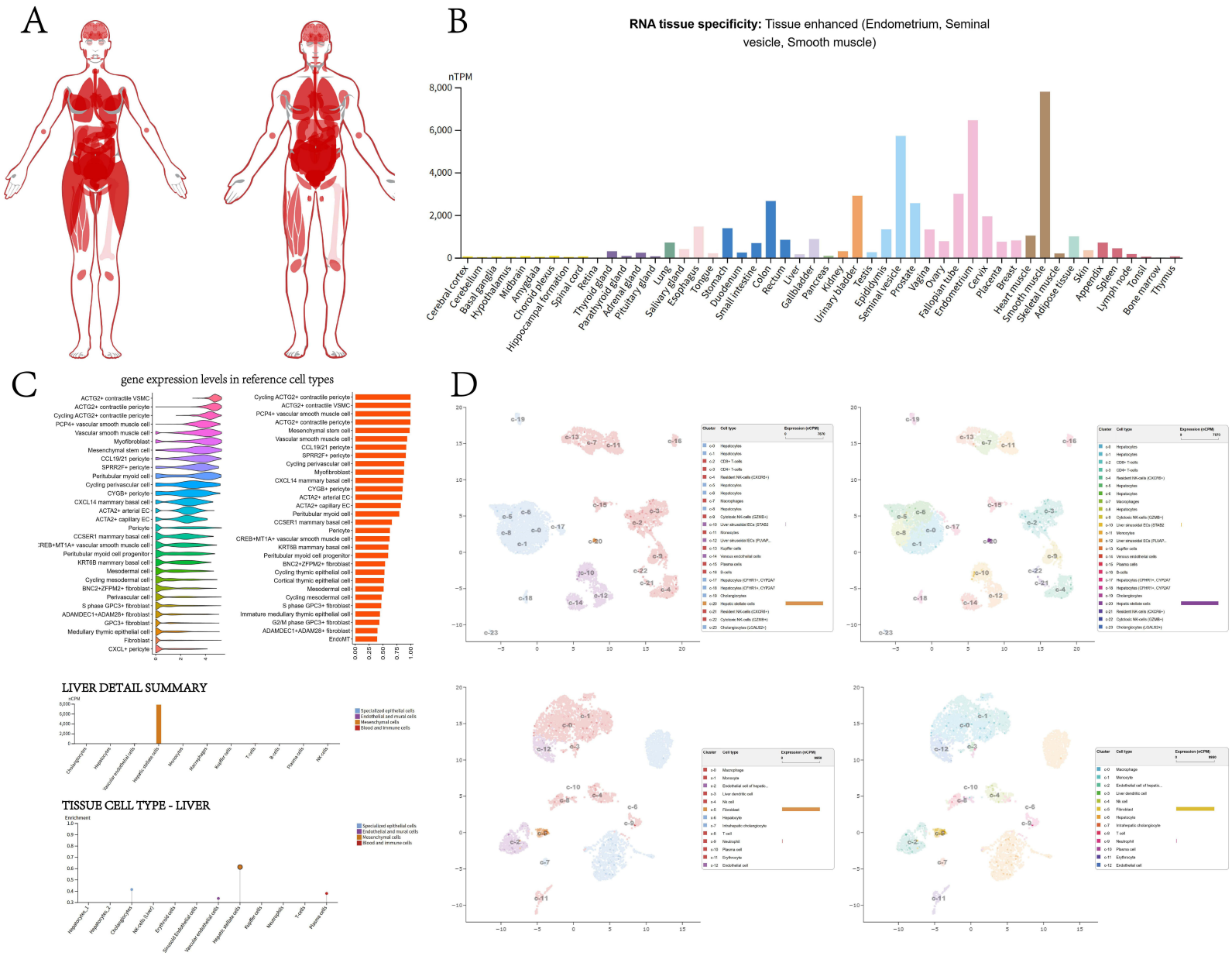

Figure 2 Expression profiles of ACTA2 across human tissues and single-cell liver datasets. (**A**) Heatmap of ACTA2 expression in human organs. (**B**) ACTA2 expressions in various tissues in the HPA database. (**C**) Gene expression levels in reference cell types. The left side is a violin plot showing expression distribution and median by cell type, and the right side is a bar chart of average expression (top 30) sorted by cell type. (**D**) Single-cell transcriptome analysis of the liver showing expression patterns across cell types and enrichment profiles.

Further integration with cell type–specific expression data from the HUSCH database indicated that ACTA2 is predominantly expressed in fibroblasts, pericytes, and smooth muscle cells (Figure 2C).

At the single-cell level (Figure 2D), analysis of HPA-derived single-cell RNA sequencing data showed that ACTA2 is preferentially expressed in hepatic stellate cells and fibroblasts, while its expression in parenchymal liver cells, including hepatocytes, Kupffer cells, and cholangiocytes, is minimal.

To further investigate hepatic expression, we analyzed single-cell and single-nucleus RNA sequencing data from the DISCO database (Figure 3A). In the liver single-cell dataset, ACTA2 transcripts were largely restricted to hepatic stellate cells, with negligible expression in hepatocytes, Kupffer cells, endothelial cells, or cholangiocytes. Single-nucleus datasets (GSM5616000, GSM5616005) yielded similar results, showing enrichment of ACTA2 in stellate and mesenchymal cell clusters, while signals in hepatocyte and immune cell clusters were negligible. These findings collectively indicate that the low overall expression of ACTA2 in normal liver tissue reflects the predominance of hepatocytes and the low proportion of fibroblasts, representing a "pseudo-low expression" driven by cellular composition rather than functional absence.

In the HUSCH liver single-cell dataset (HU_0205, GSE136103), ACTA2 exhibited pronounced cell type–specific expression (Figure 3B). UMAP clustering demonstrated that ACTA2 is primarily localized in mesenchymal cells, with near-background expression in hepatocytes, cholangiocytes, immune cells, and endothelial cells. Violin plots quantitatively confirmed that ACTA2 expression peaks significantly in mesenchymal cells. Cell–cell communication analysis revealed strong interaction between mesenchymal cells_C10 and hepatocytes_C7, as well as moderate interactions with other cell types (Figure 3B, right), suggesting that ACTA2 may play a protective role in hepatic homeostasis and tumorigenesis through mesenchymal cell–mediated intercellular communication and microenvironment regulation.

To further clarify its cell type–specific distribution, we analyzed ACTA2 expression at single-cell resolution using HPA datasets (Supplementary Figure S1A). Single-cell specificity analysis revealed differential expression of ACTA2 across cell types, with high expression in peritubular cells, smooth muscle cells, supporting cells, and myoepithelial cells of the breast, but low expression in most epithelial, immune, and neuronal cells. This pattern indicates that ACTA2 is a canonical stromal cell marker, mainly localized in cells involved in contraction and structural support.

At the protein level (Supplementary Figure S1B), HPA immunofluorescence staining showed that ACTA2 protein is primarily cytoplasmic, forming filamentous structures along actin fibers consistent with its canonical localization as α-smooth muscle actin (α-SMA). This staining pattern was confirmed across multiple cell lines (U-251 MG, A-431, U2OS), with partial co-localization with microtubule and endoplasmic reticulum (ER) markers, and minimal nuclear signal. These findings suggest that ACTA2 primarily contributes to cytoskeletal stability, cell contraction, and migration, rather than direct nuclear transcriptional regulation. Together, its cytoplasmic localization supports a potential protective role in the tumor microenvironment through regulation of cellular mechanics and matrix remodeling.

We further examined normal liver tissue images from HPA immunohistochemistry (IHC) and RNA-seq slides (Supplementary Figure S1C–D). IHC staining showed weak to moderate positivity in portal/mesenchymal and stromal regions, with consistency across individuals and antibodies, though slight variability was observed, supporting the single-cell and transcriptomic evidence of high expression in stromal/supporting cells. RNA-seq slides indicated ACTA2 signals mainly in hepatic parenchymal and stromal regions; combining this with single-cell analysis suggests that although hepatocytes express some ACTA2 transcripts, protein expression is largely restricted to structurally and motility-active stromal cells, including fibroblasts and stellate cells. This implies potential cell type–specific post-transcriptional regulation in the liver, where hepatocytes may exhibit lower translation efficiency or rapid protein degradation, whereas stromal cells maintain high protein stability to support cytoskeletal remodeling, tension maintenance, and intercellular communication.

At the genomic level (Supplementary Figure S1E–F), ACTA2 is located on chromosome 10q23.31, flanked by neighboring genes such as AL157745.5 and ACTA2-AS1. UCSC genome alignments indicate high conservation of ACTA2 across mammals, highlighting conserved exonic and regulatory regions, and underscoring its essential structural and functional roles in maintaining cytoskeletal integrity.

In summary, multi-omics evidence indicates that ACTA2 expression in the liver is mesenchymal cell–specific. The low overall expression in normal liver does not indicate functional absence but reflects the low proportion of fibroblasts

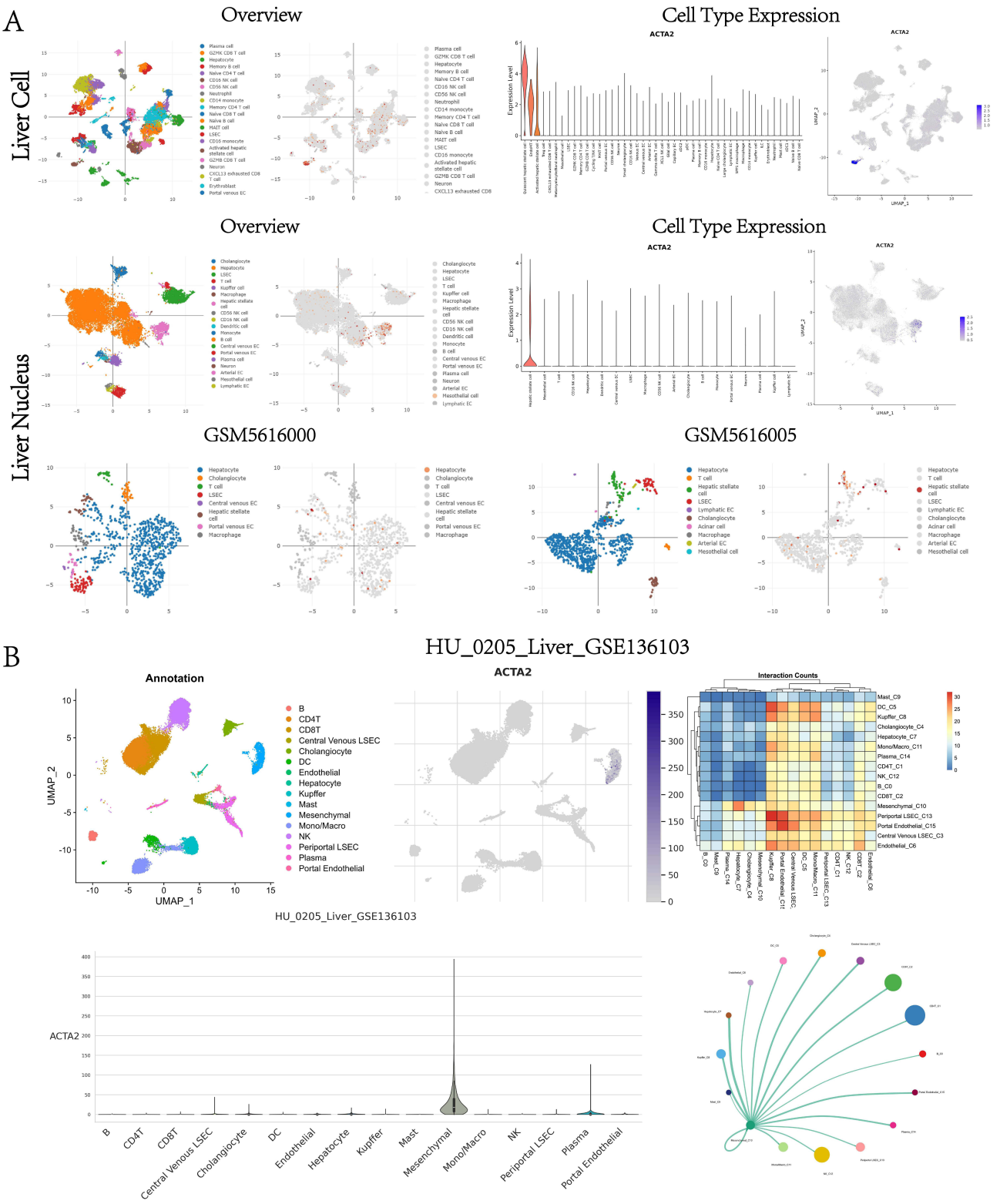

Figure 3 Liver single-cell data and intercellular interactions. (**A**) Single cell sequencing of liver cells and nuclei (GSM5616000, GSM5616005) highlighting gene expression in hepatocytes and specific subpopulations. (**B**) Expression of ACTA2 across cell types and intercellular interactions. Left: UMAP gene expression heatmap (color intensity). Bottom: Violin plot showing ACTA2 enrichment in stromal/fibroblast and smooth muscle cells. Top right: Heatmap of intercellular interaction counts (ligand–receptor pairs). Bottom right: Arc plot depicting interaction strength and directionality.

https://doi.org/10.2147/JHC.S586916

and stellate cells. ACTA2 protein localizes primarily to cytoskeletal structures in structural cells, contributing to matrix maintenance and intercellular communication. These findings provide a cellular and functional basis for ACTA2's protective role in HCC, suggesting that it may exert anti-tumor effects by maintaining hepatic microenvironment stability and limiting tumor progression.

Expression of ACTA2 in LIHC and Its Clinical Association

We utilized the TIMER2.0 database to analyze the differential expression of ACTA2 between tumor tissues and normal tissues across various cancer types. The results revealed that the RNA expression level of ACTA2 in LIHC tumor tissues was significantly higher than that in normal tissues (Figure 4A). Datasets from the BEST database further supported this conclusion (Figures 4B and C). Notably, the expression level of ACTA2 was significantly higher in female LIHC patients compared to male LIHC patients (Figure 4D). Moreover, ACTA2 was highly expressed in LIHC patients who did not respond to Sorafenib treatment, suggesting that high ACTA2 expression may be associated with Sorafenib resistance in LIHC (Figure 4E). At the protein level, ACTA2 was also significantly highly expressed in LIHC tumor tissues compared to normal tissues (Figure 4F). Survival analysis indicated that LIHC patients with high ACTA2 expression demonstrated a significantly better prognosis, as evidenced by a markedly prolonged overall survival (OS) (Figures 4G and H).

Genomic Alterations and Immune Modulatory Associations of ACTA2

To comprehensively evaluate the genomic alterations of ACTA2 and their potential immunological associations, we integrated multi-platform data from cBioPortal, TISIDB, and TIMER3.0 databases to analyze mutation patterns, copy number alterations (CNA), and structural variants in liver cancer (Supplementary Figure S2).

In the pan-cancer overview focused on liver datasets (Supplementary Figure S2A–B), ACTA2 alterations were identified in less than 1% of LIHC and related tumor samples. The predominant alteration type was structural variant, followed by gene amplification and deep deletion. Although the overall mutation frequency was low, these genomic disruptions suggest that ACTA2 integrity may be occasionally compromised, potentially influencing intracellular signaling and cytoskeletal regulation in specific tumor subsets.

To explore the potential immune-modulatory significance of ACTA2 genomic alterations, we assessed the correlation between ACTA2 CNA and immune-related gene expression using the TISIDB database (Supplementary Figure S2C). The analysis revealed no significant associations between ACTA2 copy number loss and the expression of immune checkpoint inhibitors (eg, PD-L1, CTLA4, LAG3), immune stimulators (eg, CD80, ICOS), or major histocompatibility complex (MHC) molecules (eg, HLA-A, HLA-B, HLA-C). These findings indicate that ACTA2 CNA alterations may have limited regulatory influence on immune gene expression in liver cancer, suggesting that its role in tumor immunity likely arises from non-genomic mechanisms rather than direct genetic disruption.

Additionally, we quantified ACTA2 mutation counts across datasets (Supplementary Figure S2D) and further examined its mutation and CNV status using TIMER3.0 (Supplementary Figure S2E–F). The results showed that in LIHC, ACTA2 was predominantly diploid/normal, exhibiting a low mutation rate with no notable amplifications or deletions detected. This suggests that ACTA2 maintains genomic stability in liver cancer, and its dysregulation may primarily occur at the transcriptional or post-transcriptional level, rather than through structural or copy number changes.

In summary, ACTA2 displays a stable genomic profile in liver cancer, with rare structural alterations and minimal immune associations. Although direct genomic changes appear limited, ACTA2 may still contribute to tumor progression and immune modulation through cytoskeletal remodeling, signal transduction, or metabolic adaptation pathways, underscoring its potential relevance in the molecular landscape of LIHC.

ACTA2 Mutation Site Analysis

Figure 5A shows the complete wild-type ACTA2 protein structure predicted by AlphaFold3, along with the predicted local distance difference test (pLDDT) results and the predicted aligned error (PAE), which are used to evaluate the confidence of the model's prediction for each amino acid residue position. Figure 5B shows the location of the Actin

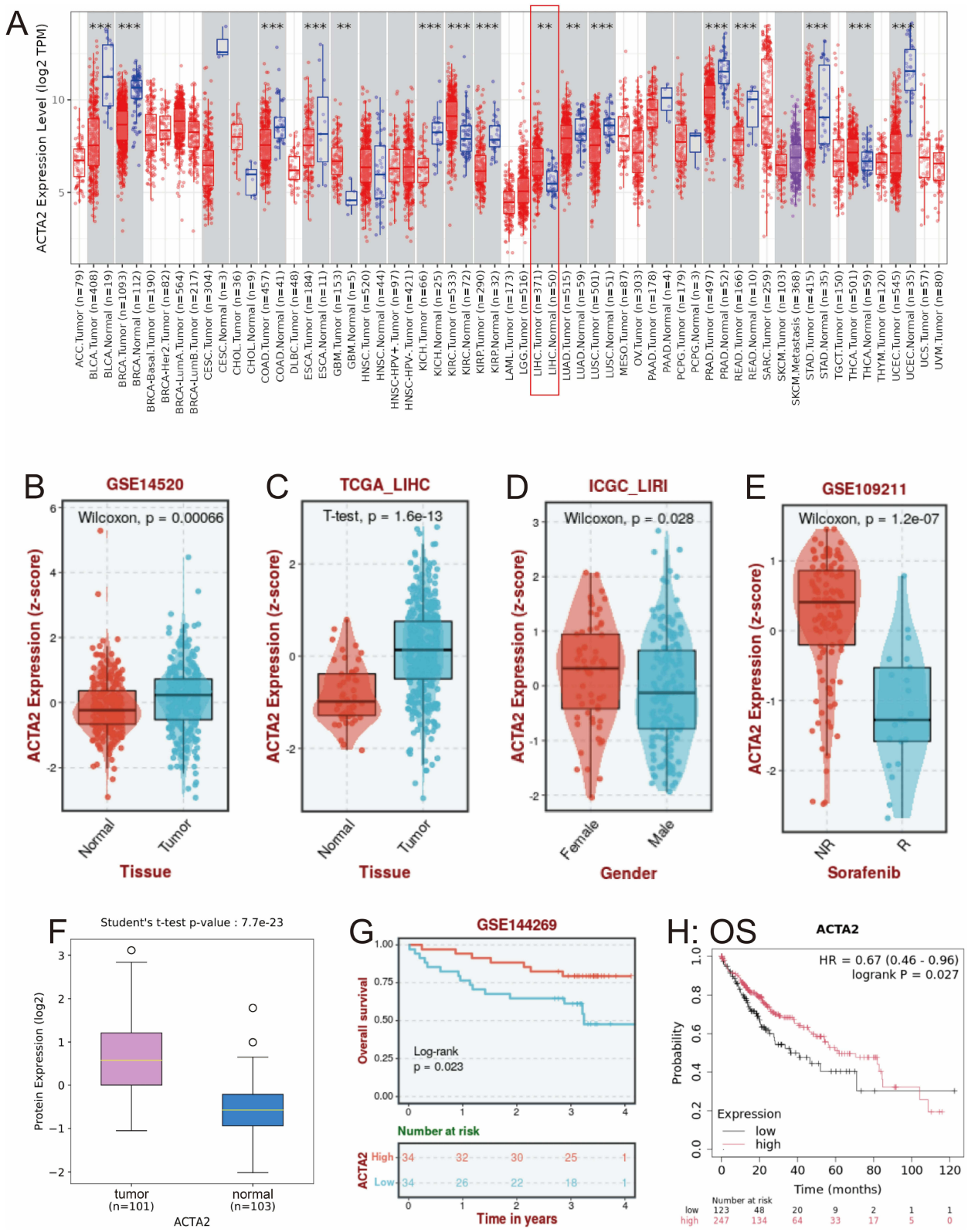

Figure 4 Expression of ACTA2 in LIHC and Its Clinical Association. (**A**) Comparison of RNA expression of ACTA2 between tumor tissues and normal tissues across various cancer types [Statistical significance was calculated using differential expression analysis (edgeR) and is indicated as follows: **p < 0.01, ***p < 0.001. The red box highlights the LIHC cohort]. (**B** and **C**) Comparison of RNA expression of ACTA2 between LIHC tumor tissues and normal tissues. (**D**) Association between ACTA2 expression and gender in LIHC patients. (**E**) Association between ACTA2 expression and response to Sorafenib treatment in LIHC patients. (**F**) Comparison of protein expression of ACTA2 between LIHC tumor tissues and normal tissues. (**G** and **H**) Kaplan-Meier curves for OS comparing high and low ACTA2 expression groups in LIHC.

https://doi.org/10.2147/JHC.S586916

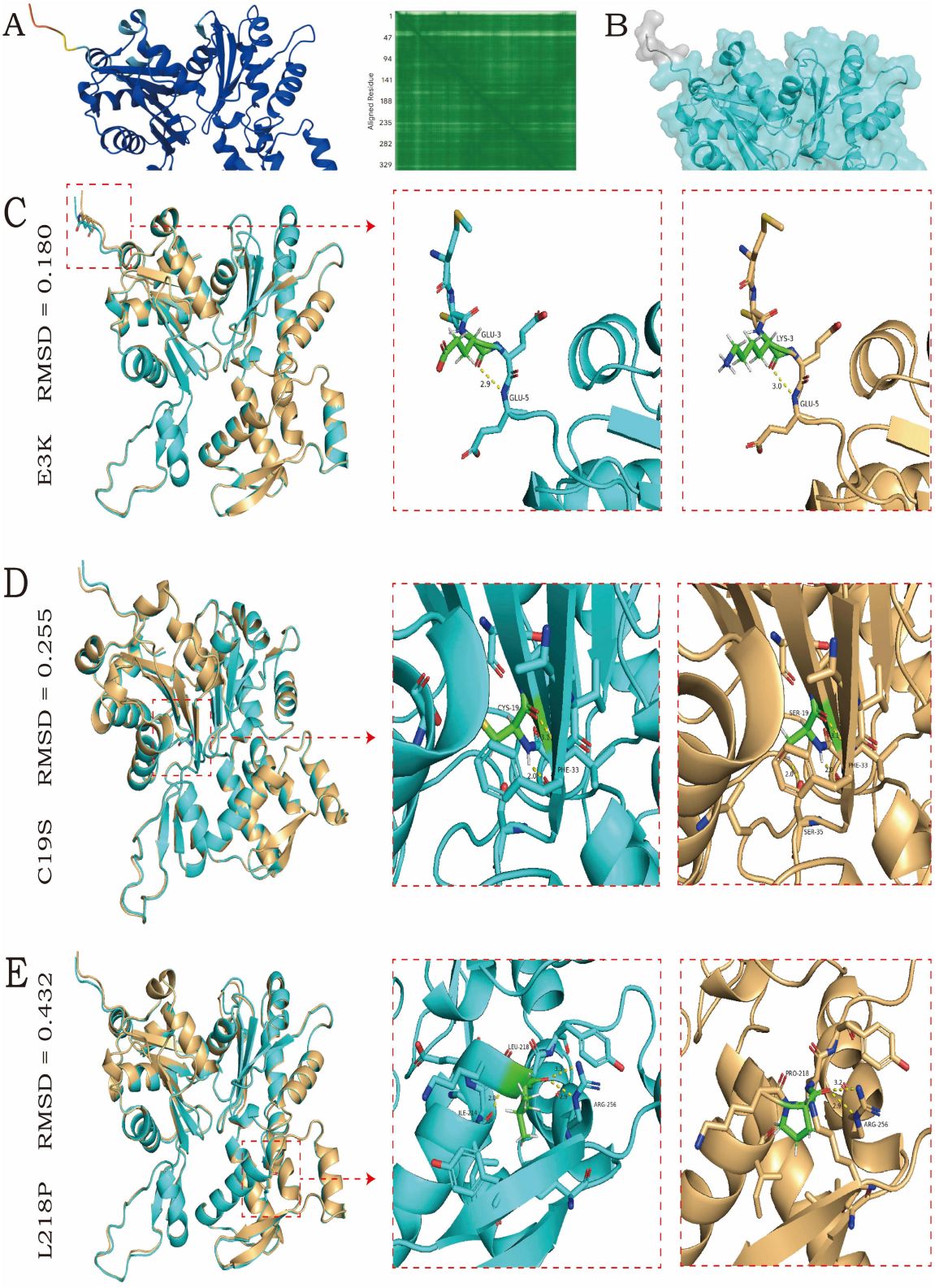

Figure 5 ACTA2 Protein Mutation Site Analysis. (**A**) Predicted ACTA2 protein structure by AlphaFold3, along with pLDDT results and PAE. (**B**) Location of the Actin domain on the ACTA2 protein, and the positions of the three mutation sites on the ACTA2 amino acid sequence. (**C**–**E**) Structural alignment of mutant and wild-type ACTA2, showing amino acid residues within 4 Å of the mutation site and associated hydrogen bonds.

https://doi.org/10.2147/JHC.S586916

domain within the ACTA2 protein and the positions of three missense mutations (E3K, C19S, L218P) identified across 3046 patients from the cBioPortal combined hepatocellular carcinoma cohort along the amino acid sequence. Figures 5C–E show the structural alignment results of the three mutant types with the wild-type protein, where the wild-type protein is shown in cyan and the mutant proteins are shown in orange. The E3K mutation is located outside the structural domain and exhibits the lowest RMSD value of 0.180 Å; the hydrogen bond between the mutation site and GLU-5 remains intact, suggesting this mutation has the least impact on the local and overall structure. The C19S mutation introduces a new hydrogen bond with SER-35, but this bond does not disrupt the core interaction network within the Actin domain. An RMSD value of 0.255 Å indicates its alteration of the overall protein conformation is at a relatively low level. The L218P mutation not only loses the inherent hydrogen bond with ILE-214 but is also constrained by the unique rigid ring structure of proline, which restricts peptide bond rotation. An RMSD value of 0.432 Å suggests this mutation causes the most significant perturbation to the overall three-dimensional structure of the protein, potentially further interfering with the biological function of ACTA2.

Immune Infiltration Analysis Data

To comprehensively investigate the relationship between ACTA2 expression and immune infiltration, we performed correlation analyses using the TIMER3.0 and TISIDB databases (Figure 6).

In the TIMER3.0 analysis (Figure 6A), ACTA2 expression exhibited significant associations with multiple immune and stromal cell types. Overall, ACTA2 showed heterogeneous correlations with $CD8^+$ T cells, $CD4^+$ T cells, and NK cells, with both positive and negative associations observed across different estimation algorithms, as indicated by mixed red and blue regions ($p < 0.05$), suggesting a context-dependent relationship rather than a uniform effect on immune surveillance and cytotoxic responses. Additionally, moderate positive correlations were observed with dendritic cells and macrophages, which contribute to antigen presentation and immune activation.

ACTA2 expression displayed strong positive correlations with CAFs and endothelial cells, as reflected by predominantly red-colored grids, consistent with its established role as a stromal-associated gene. Weak or non-significant correlations were observed for neutrophils and mast cells, indicating limited or dataset-dependent associations rather than direct regulatory effects on these cell populations. Collectively, these findings demonstrate that ACTA2 is positively associated with stromal components and exhibits variable associations with immune cell infiltration, suggesting a context-dependent role in the tumor microenvironment rather than a direct suppressive effect on stromal or immune components.

In the TISIDB analysis (Figure 6B), we further examined the relationship between ACTA2 expression and immune regulatory gene sets. ACTA2 expression showed an overall positive correlation with genes associated with lymphocyte infiltration, particularly those related to T-cell chemotaxis and activation. Within the immunostimulator module, ACTA2 was variably correlated across different genes, with moderate positive associations observed for selected molecules such as ENTPD1, TMEM173, and CD48, indicating a heterogeneous pattern rather than a uniform activation signature. In contrast, within the immunoinhibitor module, ACTA2 exhibited generally weak and heterogeneous correlations across genes, without a consistent positive or negative pattern, suggesting a context-dependent relationship with immunosuppressive signaling pathways.

Furthermore, within the MHC molecule module, ACTA2 exhibited generally weak to moderate positive correlations with genes such as HLA-A, HLA-B, and HLA-E, indicating a potential association with antigen presentation capacity rather than a uniformly strong effect. Similar variable positive associations were observed in the chemokine module, notably with CCL5, CXCL9, and CXCL12, which are key mediators of cytotoxic lymphocyte recruitment. In contrast, correlations within the receptor module were generally weak, suggesting that ACTA2 may be more closely associated with cytokine–chemokine interaction patterns rather than direct receptor-mediated signaling.

Taken together, these analyses reveal that ACTA2 expression is closely linked to stromal composition and displays context-dependent relationships with immune regulatory networks in liver cancer, displaying heterogeneous correlations across gene modules rather than a uniform activation pattern. These findings suggest that ACTA2 expression reflects tumor microenvironment characteristics, rather than directly promoting immune activation or suppression.

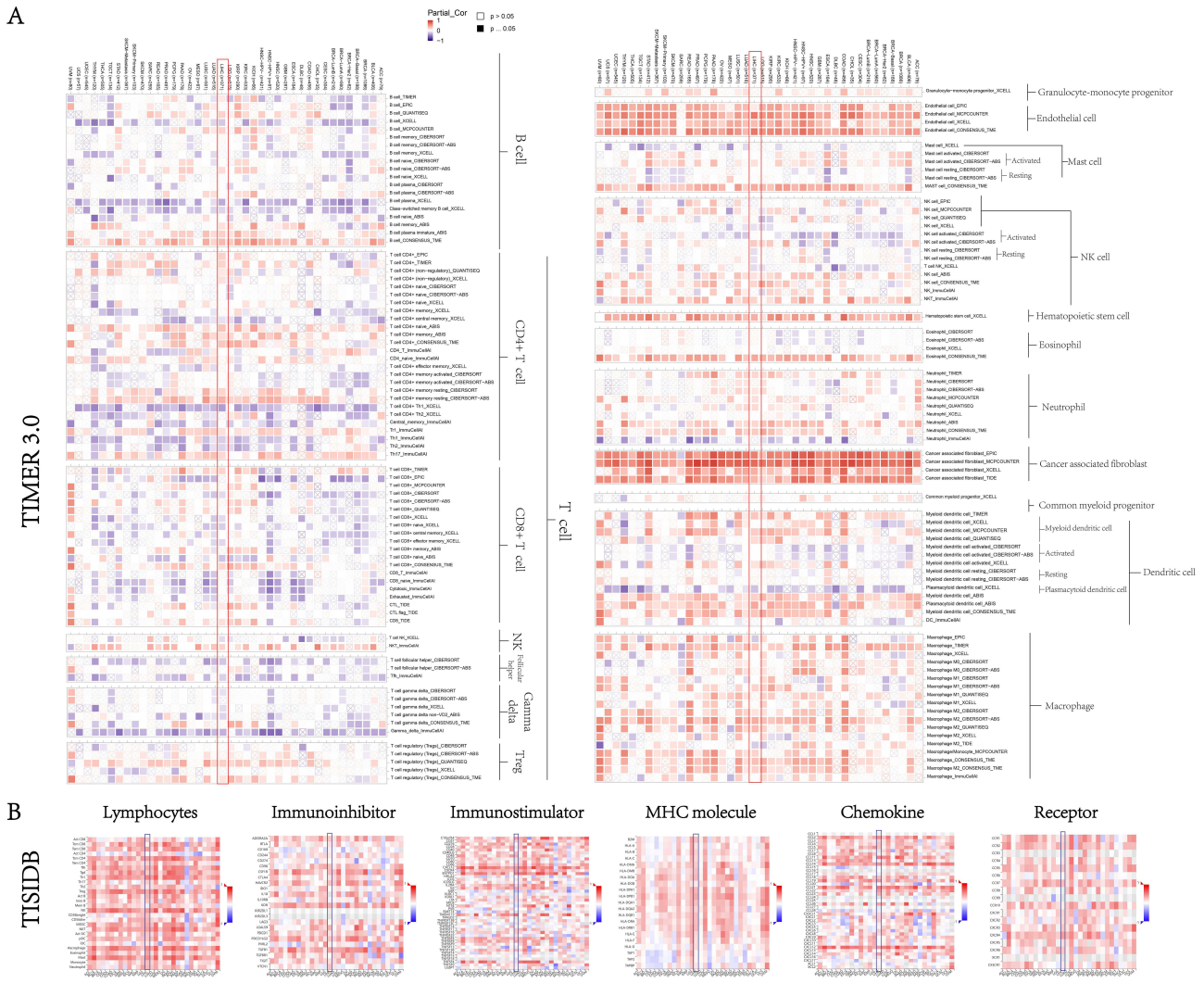

Figure 6 Correlation between ACTA2 expression and immune cell infiltration and immune molecules. (**A**) TIMER3.0-based pan-cancer analysis of the association between ACTA2 expression and immune cell infiltration. Color intensity represents the partial correlation coefficient (red, positive; blue, negative), and filled squares indicate statistical significance ($p < 0.05$). The red vertical frames mark the LIHC cohort. Filled squares indicate statistical significance ($p < 0.05$), while crossed-out squares indicate non-significant associations ($p \geq 0.05$). (**B**) TISIDB analysis shows correlations between ACTA2 expression and immune-related gene modules, including lymphocytes, immunoinhibitors, immunostimulators, MHC molecules, chemokines, and receptors. The blue highlighted boxes denote the LIHC cohort analyzed in this study.

Single-Cell RNA-Seq Analysis

In the three LIHC single-cell datasets obtained from the TISCH2 database (GSE125449-Figure 7A, GSE146409-Figure 7B, and GSE166635-Figure 7C), UMAP visualizations revealed that tumor tissues were primarily composed of malignant epithelial cells, fibroblasts, endothelial cells, T/NK cells, B cells, and myeloid cells. ACTA2-overlaid UMAP feature plots and violin plots consistently showed that high ACTA2 expression was almost exclusively restricted to fibroblast clusters, with negligible expression in malignant cells, hepatocytes, or immune cells. This indicates that ACTA2 serves as a relatively specific marker for fibroblasts within the LIHC tumor microenvironment.

Cell–cell interaction heatmaps demonstrated extensive ligand–receptor communication between fibroblasts and malignant epithelial cells, endothelial cells, and multiple immune cell subsets. In the GSE166635 dataset, epithelial cells also exhibited substantial outgoing signaling activity. The fibroblast-centered outward signaling chord diagrams further revealed that fibroblasts send extensive signals to diverse cell populations, underscoring their pivotal role in maintaining and remodeling the tumor microenvironment.

In the GSE149614 dataset (Figure 7D), the integrated UMAP plot similarly showed that ACTA2-positive cells were predominantly localized within fibroblast clusters. Its expression in all other cell types remained at near-background

https://doi.org/10.2147/JHC.S586916

https://doi.org/10.21147/j.HC.S586916

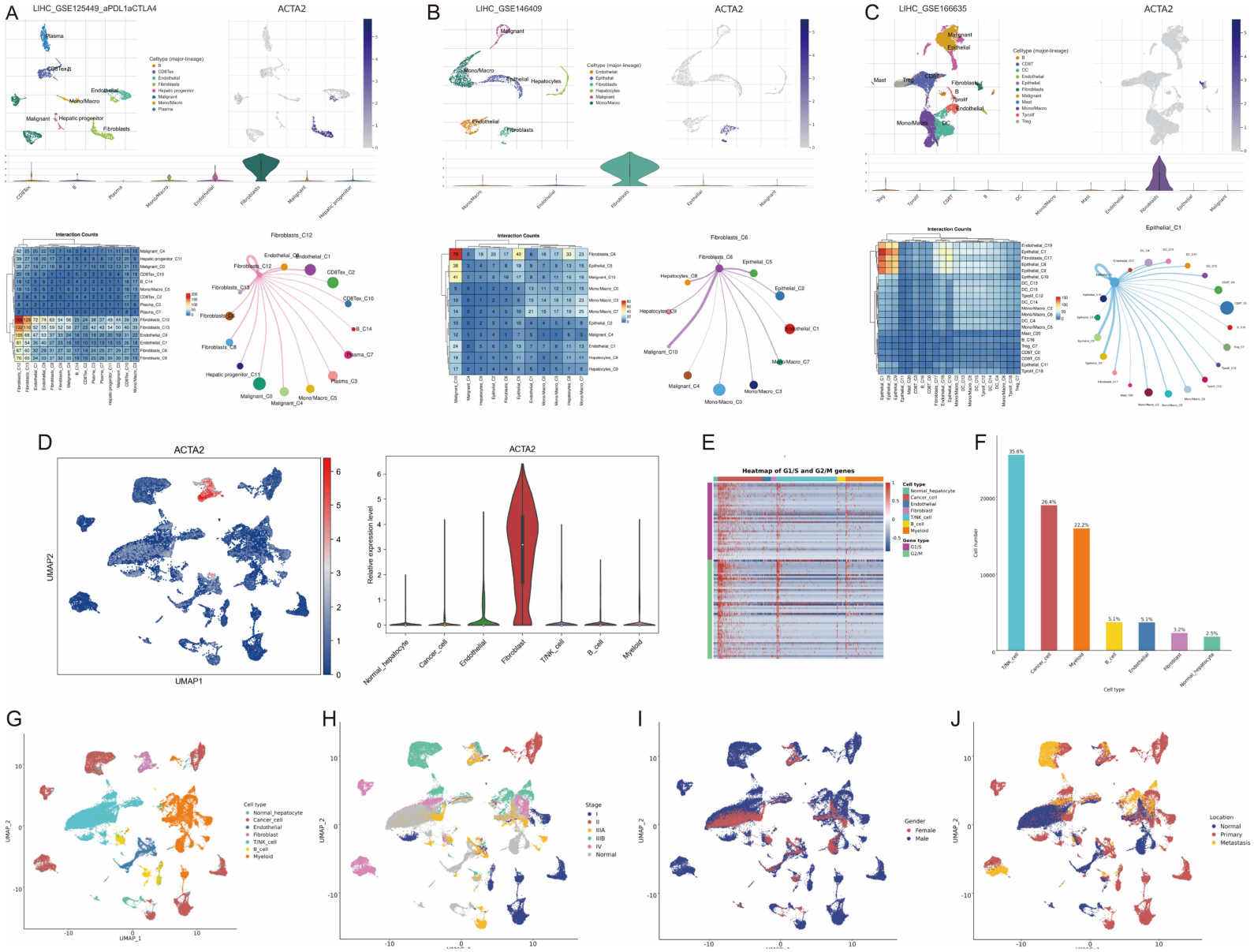

Figure 7 Single-cell RNA-seq analysis. (**A**–**C**) Analysis results of three LIHC single-cell datasets (GSE125449, GSE146409, and GSE166635) from the TISCH2 database. Shown are the UMAP plots annotated by cell type (upper left), ACTA2-overlaid UMAP feature plots (upper right), violin plots depicting ACTA2 expression across cell types (middle), cell–cell interaction heatmaps (lower left), and fibroblast-centered outward signaling chord diagrams (lower right). (**D**) UMAP feature plot of ACTA2 expression (left) and violin plot of ACTA2 expression across cell types (right) in the GSE149614 dataset from the scCancerExplorer database. (**E**) Heatmap of G1/S and G2/M phase cell cycle–related gene expression across different cell types in the GSE149614 dataset. (**F**) Bar plot showing the number and proportion of major cell types in the GSE149614 dataset. (**G**–**J**) UMAP plots of the GSE149614 dataset recolored by cell type (**G**), tumor stage (**H**), sex (**I**), and sampling location (**J**).

levels, which was again supported by the violin plot. The cell cycle heatmap (Figure 7E) indicated that multiple cell types expressed varying levels of G1/S and G2/M phase–related genes, suggesting heterogeneous proliferative activity within the tumor microenvironment. The cell-type composition bar plot (Figure 7F) showed that T/NK cells, malignant epithelial cells, and myeloid cells constituted the three largest populations, accounting for approximately 35.6%, 26.4%, and 22.7% of cells, respectively. B cells and endothelial cells each contributed around 5.1%, while fibroblasts and normal hepatocytes were less abundant (approximately 3.2% and 2.5%).

UMAP recoloring for GSE149614 showed distinct clustering of major cell types (Figure 7G), whereas recoloring by tumor stage (Figure 7H) revealed substantial intermixing across different stages, suggesting shared transcriptional features among samples with different clinical stages. Coloring by sex (Figure 7I) demonstrated highly overlapping distributions between male- and female-derived cells, with no obvious sex-related spatial separation. Coloring by sampling location (Figure 7J) showed that cells from normal tissues tended to localize to specific regions, while primary and metastatic tumor cells were intermingled across multiple clusters, indicating certain transcriptional continuity between primary and metastatic lesions.

Collectively, these results show that ACTA2 is robustly and specifically expressed in fibroblasts across multiple LIHC single-cell datasets. $ACTA2^{+}$ fibroblasts engage in extensive ligand–receptor interactions with surrounding malignant and immune cells, suggesting that they may serve as key effector cells involved in the modulation of the LIHC tumor microenvironment.

Enrichment Analyses Link ACTA2 to Pro-Tumorigenic Pathways in LIHC

To investigate the biological pathways associated with ACTA2 in LIHC, we compared gene expression profiles of LIHC tumors with high vs. low ACTA2 expression. KEGG pathway analysis of differentially expressed genes (DEGs) between ACTA2-high and ACTA2-low tumors revealed significant enrichment of pathways related to cell growth and the tumor microenvironment. Notably, genes upregulated in ACTA2-high samples mapped to the PI3K–Akt signaling pathway, focal adhesion, ECM–receptor interaction, and other signaling cascades relevant to cell survival and adhesion (Figure 8A). These results suggest that high ACTA2 expression is associated with an activated extracellular matrix and pro-survival signaling milieu in liver cancer.

Consistent with the KEGG findings, Gene Ontology (GO) enrichment analysis highlighted that ACTA2-linked DEGs participate in remodeling of the tumor microenvironment and cytoskeletal organization. In the Biological Process category, terms such as extracellular matrix organization, collagen fibril organization, cell adhesion, and muscle system process were over-represented in the ACTA2-associated gene set. Enriched Cellular Component terms pointed to the extracellular region and the contractile fiber apparatus, while Molecular Function enrichment included actin binding and integrin binding activities (Figure 8B). These GO results underscore the connection between ACTA2 and processes like extracellular matrix remodeling, cell motility, and contractile function, which can facilitate cancer progression.

To validate and further explore these associations, we performed gene set enrichment analysis (GSEA). GSEA using the KEGG gene set library confirmed a significant positive enrichment of the PI3K–Akt signaling pathway gene set in tumors with high ACTA2 expression (enrichment normalized score > 1, $q < 0.05$), as well as enrichment of pathways related to cell motility such as focal adhesion and regulation of the actin cytoskeleton (Figure 8C). Similarly, GSEA of GO Biological Process gene sets revealed that high ACTA2 expression was positively correlated with gene sets involved in extracellular structure organization, wound healing, and angiogenesis, reflecting a pro-invasive and pro-angiogenic program, whereas gene sets related to liver metabolic processes were comparatively downplayed (Figure 8D).

Together, these enrichment analyses indicate that ACTA2 upregulation in LIHC is closely associated with pathways that promote tumor aggressiveness – including activation of the PI3K–Akt survival pathway, enhancement of cell-matrix adhesion, and extensive remodeling of the extracellular matrix. This suggests that ACTA2 may contribute to LIHC progression by fostering a tumor microenvironment conducive to growth, invasion, and angiogenesis.

Molecular Simulations Reveal Stable TCDD Binding to ACTA2 and Altered Protein Dynamics

To characterize the binding of TCDD to ACTA2, we performed a 100 ns MD simulation on the ACTA2–TCDD complex (starting from the best docking pose) alongside an apo ACTA2 control simulation. The RMSD trajectories showed that the

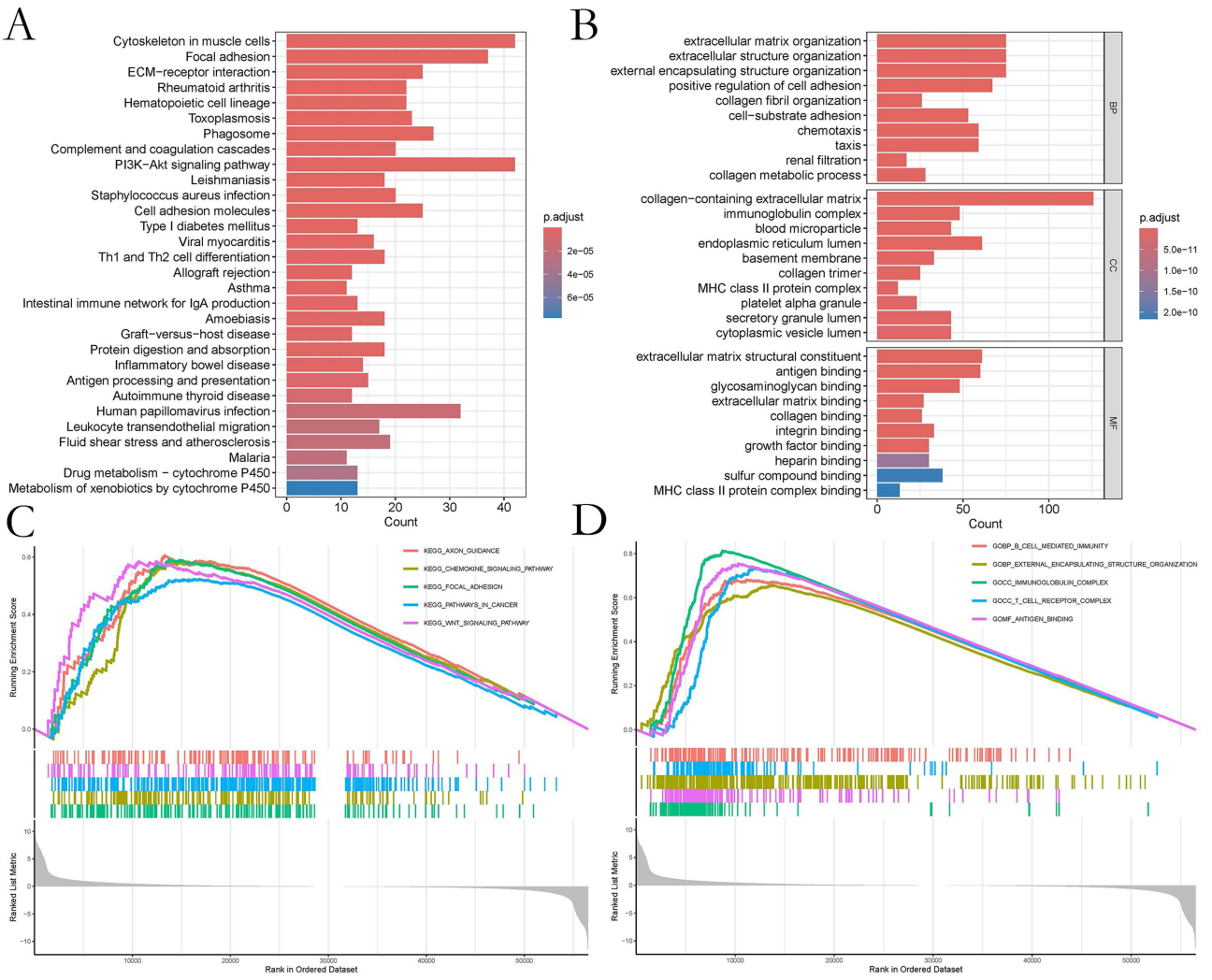

Figure 8 Functional enrichment analysis of ACTA2-associated genes in LIHC. (**A**) KEGG pathway enrichment analysis of differentially expressed genes between high-ACTA2 and low-ACTA2 hepatocellular carcinoma samples. The dot plot displays significantly enriched pathways (adjusted $p < 0.05$), with point size indicating gene count and color intensity reflecting the statistical significance. Key enriched pathways include PI3K–Akt signaling, focal adhesion, and ECM–receptor interaction, among others associated with tumor progression. (**B**) Gene Ontology (GO) enrichment results for genes correlated with ACTA2 expression, covering Biological Processes (BP), Cellular Components (CC), and Molecular Functions (MF). The circular bar chart highlights top GO terms, such as extracellular matrix organization (BP), contractile fiber and actin cytoskeleton (CC), and actin binding (MF), implicating ACTA2 in processes of matrix remodeling and cytoskeletal structure. (**C**) Gene set enrichment analysis (GSEA) plot based on the KEGG gene set database, showing a positive enrichment of ACTA2-high samples for PI3K–Akt signaling and other oncogenic pathways. The enrichment curve for PI3K–Akt signaling is shown as an example, with the gene set enrichment score profile and leading-edge subset indicated. (**D**) GSEA enrichment plot based on GO Biological Process gene sets, illustrating significant enrichment of processes such as extracellular structure organization and cell adhesion in ACTA2-high tumors. The plot depicts one representative GO process (e.g, extracellular matrix organization) enriched in the high ACTA2 group, with the running enrichment score and the positions of its genes in the ranked gene list. In both GSEA analyses, a normalized enrichment score > 1 and FDR $q < 0.05$ denote statistically significant enrichment.

ACTA2–TCDD complex attained equilibrium with smaller structural fluctuations compared to apo ACTA2, suggesting that TCDD binding confers enhanced conformational stability to the actin protein (Figure 9A). Consistently, per-residue RMSF analysis revealed that most regions of ACTA2 exhibit similar flexibility with and without ligand, with only minor dampening of fluctuations observed in loop regions surrounding the TCDD binding site (Figure 9B). The overall compactness of the protein, measured by the radius of gyration (R_g), was slightly increased (lower R_g) in the TCDD-bound state, indicating that ACTA2 adopts a marginally more compact conformation upon ligand binding (Figure 9C).

Dynamic intermolecular interactions were evident throughout the simulation. The number of hydrogen bonds between ACTA2 and TCDD remained steady over time, with at least 1–2 persistent hydrogen bonds present during most of the 100 ns trajectory (Figure 9D). This stable hydrogen-bonding, along with hydrophobic contacts (predominantly between TCDD's aromatic rings and hydrophobic pockets of ACTA2), contributed to the maintenance of the bound complex. Correspondingly,

exploration of the free energy landscape (FEL) further supported the stability of the ligand-bound state. The ACTA2–TCDD complex sampled a narrower and deeper energy basin relative to apo ACTA2, indicating that the TCDD-bound ACTA2 resides in a more energetically favorable conformational ensemble (Figure 9E and F). Representative structural snapshots taken at 0 ns, 50 ns, and 100 ns illustrate that TCDD remains stably lodged within the ACTA2 binding pocket over the course of the simulation, with no significant dissociation or reorientation (Figure 9G i–G ii).

Post-simulation binding free energy calculations corroborated the strong affinity of TCDD for ACTA2. MM/GBSA analysis yielded a markedly negative average ΔG_{bind}, confirming that complex formation is energetically favorable. Decomposition of the binding energy revealed substantial contributions from van der Waals interactions (due to the snug fit of TCDD's chlorinated aromatic rings in the hydrophobic cleft of ACTA2) and from electrostatic interactions (including the aforementioned hydrogen bonds), whereas polar solvation opposed binding to a lesser extent (Figure 9H i–H ii). Finally, the docked binding mode refined by MD is depicted in Figure 9I. The final ACTA2–TCDD structural model shows TCDD (rendered in green) snugly bound in a pocket on the ACTA2 surface, with a predicted binding affinity of approximately –7.05 kcal/mol. Collectively, these results demonstrate that TCDD forms a stable and energetically favorable complex with ACTA2, potentially influencing ACTA2's conformation and function

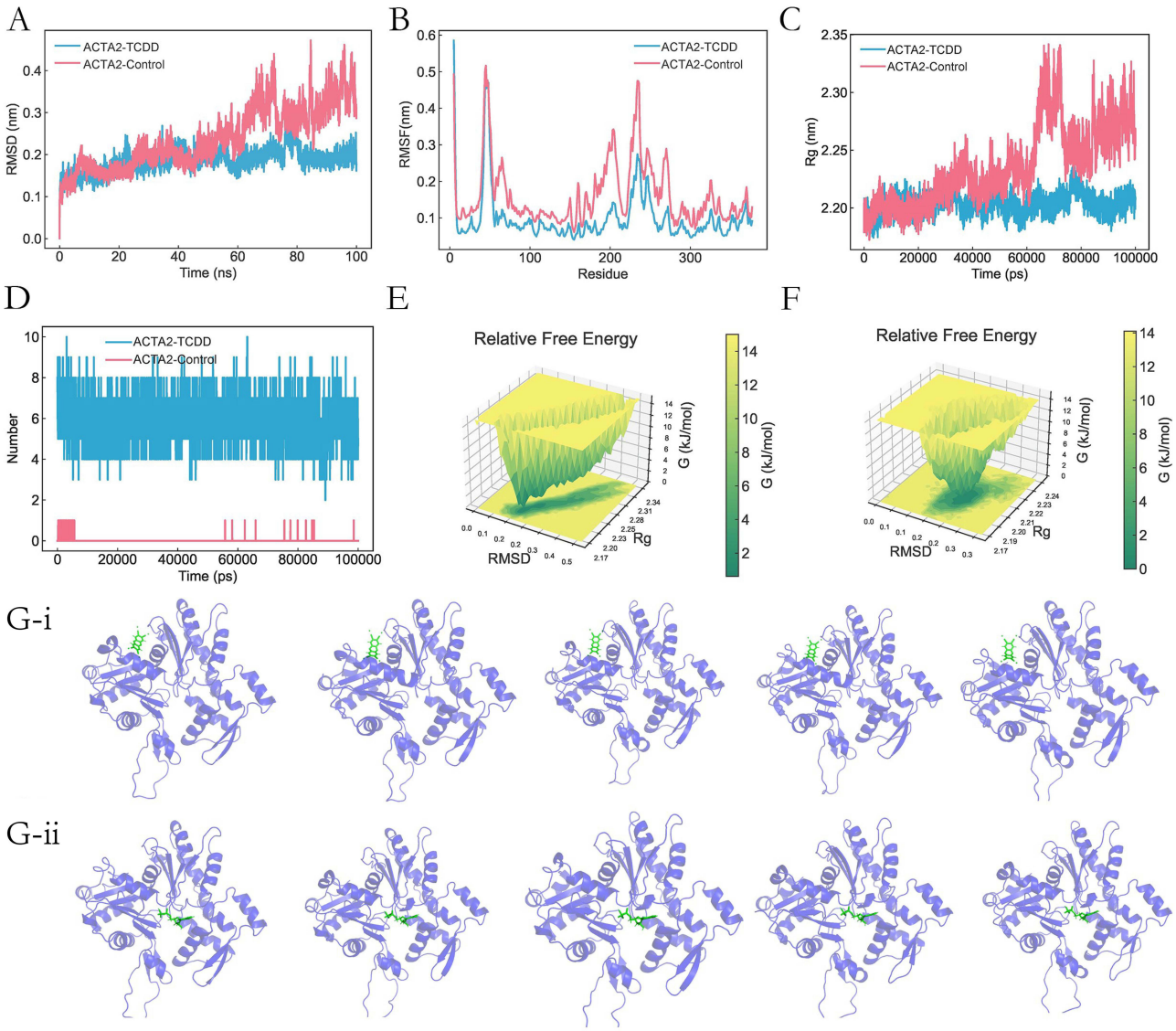

Figure 9 Continued.

https://doi.org/10.2147/JHC.S586916

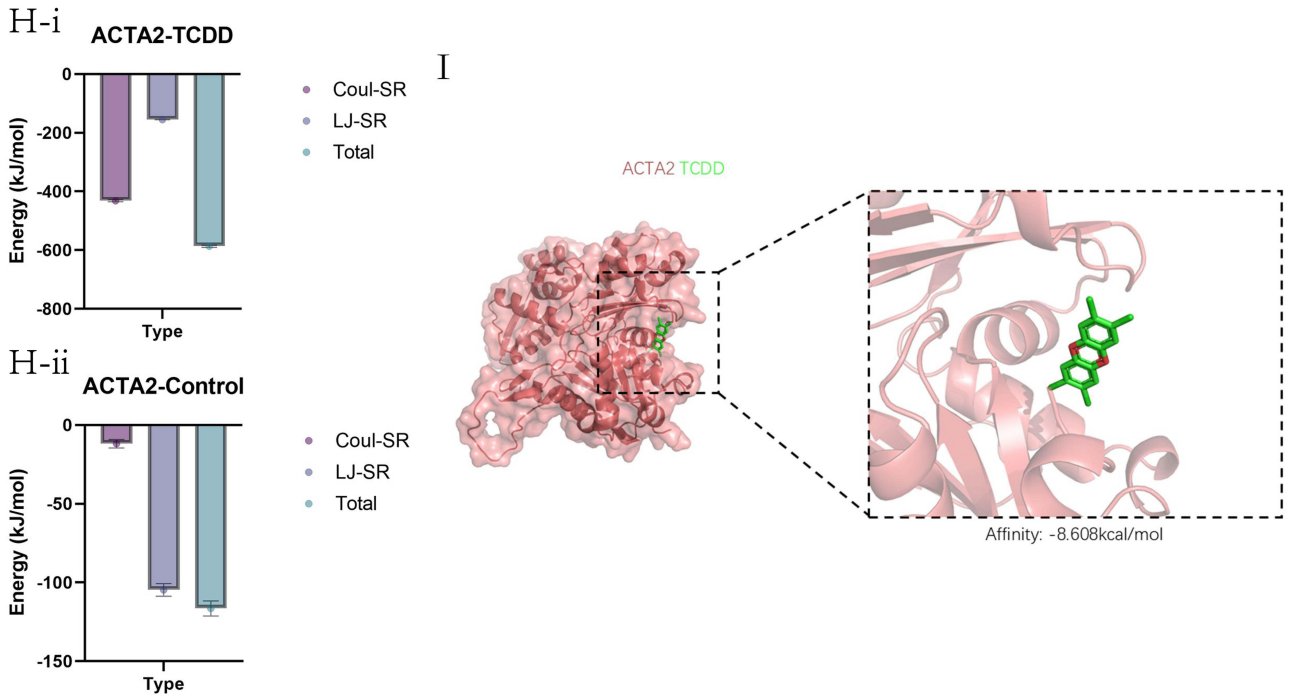

Figure 9 Molecular dynamics simulations of ACTA2–TCDD interaction. (**A**) Backbone RMSD trajectories of ACTA2 in the apo (ligand-free) state and in complex with TCDD over a 100 ns MD simulation. The ACTA2–TCDD complex shows a stabilized RMSD relative to apo ACTA2, indicating convergence to a stable bound conformation. (**B**) Per-residue RMSF of ACTA2 in the absence and presence of TCDD, highlighting that overall protein flexibility is similar between the two conditions. Slight reductions in mobility are evident at residues lining the TCDD binding interface for the complex. (**C**) Radius of gyration (R_g) as a function of simulation time for apo ACTA2 versus the ACTA2–TCDD complex. A modest decrease in R_g upon TCDD binding reflects a small increase in the compactness of the ACTA2 structure when the ligand is bound. (**D**) Time evolution of the number of hydrogen bonds between ACTA2 and TCDD throughout the simulation. The ligand–protein complex maintains 1–3 persistent hydrogen bonds during most of the trajectory, supporting the stability of TCDD's binding. (**E** and **F**) Free energy landscapes (FEL) of ACTA2 sampled during MD, projected onto two collective variables (RMSD and R_g). (**E**) FEL of apo ACTA2 shows a broader, shallower energy basin, whereas (**F**) the ACTA2–TCDD complex exhibits a narrower and deeper minimal energy basin, indicating that TCDD binding restricts ACTA2 to more favorable conformational states. Warmer colors (red/yellow) indicate higher probability (lower free energy) regions. (**G**-i, **G**-ii) Representative structural snapshots from the simulations. (**G**1) Apo ACTA2 at 0 ns and 100 ns, illustrating the baseline conformation of the protein. (**G**2) ACTA2–TCDD complex at 0 ns and 100 ns, showing TCDD (green spheres or sticks) stably lodged in the ACTA2 binding pocket throughout the simulation with minimal displacement. (**H**-i, **H**-ii) MM/GBSA binding free energy decomposition for the ACTA2–TCDD interaction. Bar charts illustrate the contributions of electrostatic (Coulomb) and van der Waals interactions, as well as polar and nonpolar solvation energies. (**H**1) Energetic profile of the apo ACTA2 reference state and (**H**2) the ACTA2–TCDD complex. The strong negative total ΔG_{bind} for the complex is driven predominantly by favorable van der Waals and Coulomb interactions, partially offset by polar solvation costs. (**I**) Final structural model of the ACTA2–TCDD complex after MD refinement. TCDD (green) is shown nestled in a hydrophobic cleft of ACTA2 (surface representation), with key contact residues surrounding the ligand. The docking-predicted binding affinity for this pose is approximately –7.05 kcal/mol, supporting a high-affinity interaction.
Abbreviations: RMSD, root mean square deviation; RMSF, root mean square fluctuation.

in the cell, the molecular docking and MD simulation results are theoretical and exploratory, and that their physiological and clinical significance should be interpreted cautiously pending further experimental validation.

TCDD Induces ACTA2-Dependent Proliferation and PI3K/Akt Signaling in LX-2 (ACTIVE) and CAF Cells

We next investigated the in vitro effects of TCDD on liver tumor–associated stromal cells and the role of ACTA2 in mediating these effects. CCK-8 cell viability assays showed that TCDD exposure significantly promoted the proliferation of LX-2 (ACTIVE) cells and CAFs in a dose- and time-dependent manner (Figure 10A).

To determine whether ACTA2 is involved in this TCDD-driven proliferation, we examined ACTA2 expression and manipulated its levels. qRT-PCR analysis revealed that TCDD treatment downregulated ACTA2 mRNA expression in LX-2 (ACTIVE) and CAF cells in a concentration-dependent fashion (Figure 10B). Consistently, cells transfected with the ACTA2 overexpression plasmid (Ov-ACTA2) exhibited a robust increase in ACTA2 transcripts and protein relative to vector control cells, confirming the efficiency of ACTA2 overexpression. Notably, in ACTA2-overexpressing cells, TCDD treatment did not further enhance ACTA2 expression, suggesting that ACTA2 levels were already saturated by plasmid-mediated overexpression (Figure 10B).

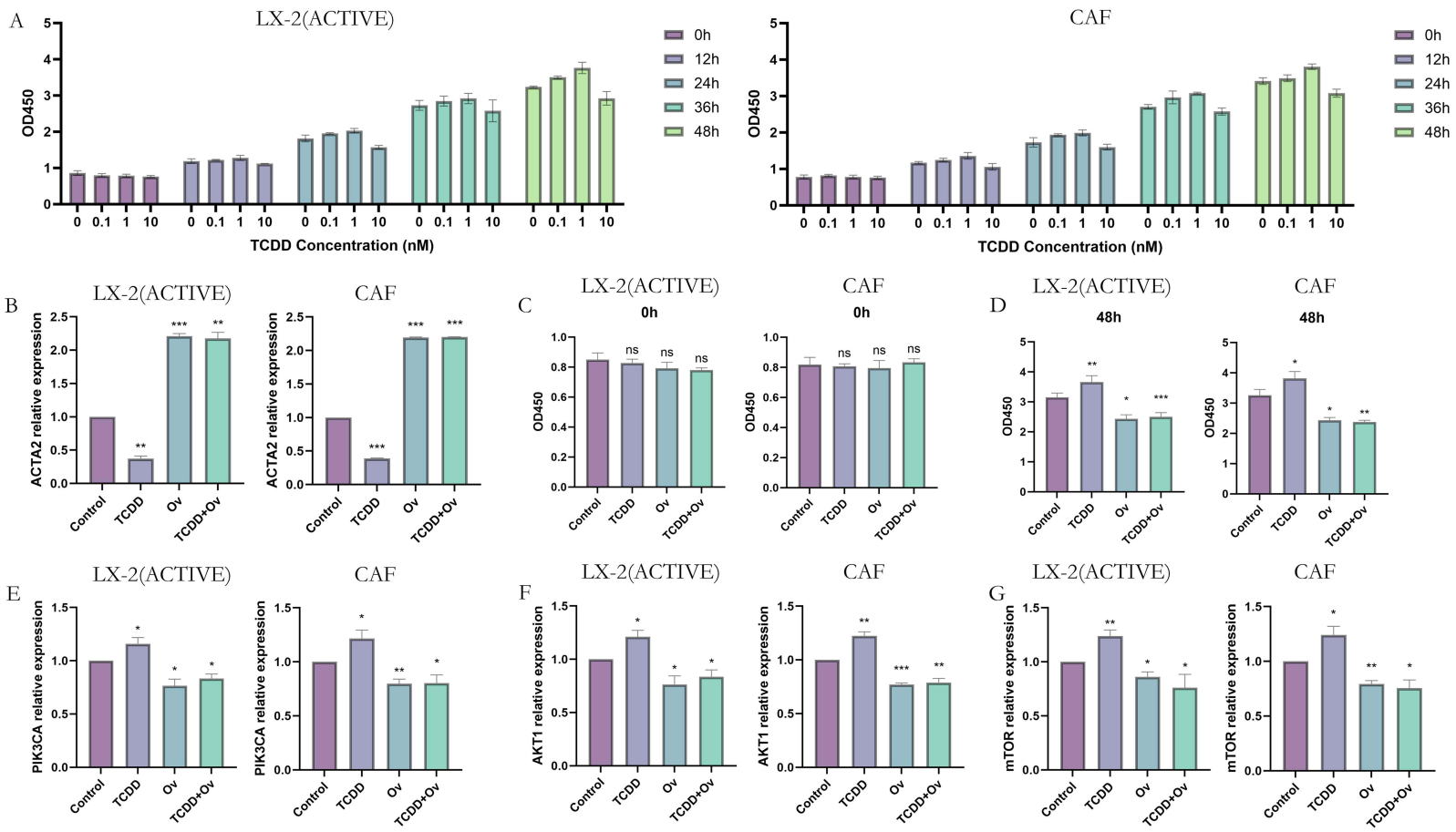

Figure 10 TCDD promotes proliferation and PI3K/Akt pathway activation in LX-2 (ACTIVE) cells and CAFs through ACTA2. (**A**) CCK-8 assay showing the proliferation of LX-2 (ACTIVE) cells and CAFs treated with TCDD at 0, 0.1, 1, and 10 nM over 0–48 h. Cell viability (absorbance at 450 nm) increased with higher TCDD concentrations and longer exposure times, indicating a dose- and time-dependent proliferative effect. (**B**) Relative ACTA2 mRNA expression in LX-2 (ACTIVE) cells and CAFs under different conditions: TCDD treatment (1 nM, 24 h), plasmid-mediated ACTA2 overexpression (Ov-ACTA2), and the combination of ACTA2 overexpression plus TCDD treatment (TCDD+Ov). TCDD alone upregulates ACTA2 expression, whereas Ov-ACTA2 further increases ACTA2 levels. In ACTA2-overexpressing cells, additional TCDD stimulation does not significantly enhance ACTA2 expression compared with Ov-ACTA2 alone, indicating that ACTA2 expression is saturated by plasmid overexpression. (**C** and **D**) Cell viability at the start (0 h) and end (48 h) of treatment under four conditions: Control (no TCDD, no plasmid), TCDD (1 nM), ACTA2 overexpression (Ov-ACTA2), and combined ACTA2 overexpression + TCDD (TCDD+Ov). (**C**) Viability at 0 h confirms comparable initial cell numbers among groups. (**D**) After 48 h, TCDD-treated cells show significantly higher viability than control, while ACTA2 overexpression alone reduces viability. Notably, cells with ACTA2 overexpression + TCDD do not exhibit the proliferation seen with TCDD treatment alone, indicating that enforced ACTA2 expression attenuates TCDD-driven growth. (**E–G**) Relative mRNA expression levels of PIK3CA, AKT1, and MTOR (key components of the PI3K/Akt/mTOR pathway) measured by qRT-PCR in the same four groups (Control, TCDD, Ov-ACTA2, and TCDD+Ov). TCDD treatment markedly upregulates PIK3CA (E), AKT1 (F), and MTOR (**G**) expression compared to control, consistent with activation of the PI3K/Akt pathway. ACTA2 overexpression significantly lowers the expression of these genes, and the combination of ACTA2 overexpression with TCDD yields expression levels similar to overexpression alone (with no rescue by TCDD), demonstrating that ACTA2 overexpression blunts TCDD-induced activation of this signaling axis in LX-2 (ACTIVE) cells and CAFs. Data in panels B, D, and E–G are presented as mean ± SEM of three independent experiments. Statistical significance: *$p < 0.05$, **$p < 0.01$, ***$p < 0.001$ compared to the appropriate control; "ns" indicates no significant difference ($p \geq 0.05$).

https://doi.org/10.2147/JHC.S586916

Functionally, ACTA2 overexpression significantly attenuated the pro-proliferative effect of TCDD in both LX-2 (ACTIVE) cells and CAFs. In the context of enforced ACTA2 expression, TCDD could no longer promote cell growth: ACTA2-overexpressing cells treated with TCDD showed no significant increase in viability compared with ACTA2-overexpressing cells without TCDD, and their viability remained significantly lower than that of control cells exposed to TCDD (Figure 10C and D). Even at a low concentration of 0.1 nM, TCDD elicited a measurable increase in cell viability over 48 hours. By 48 h post-treatment, TCDD at 1 nM markedly enhanced the viability of both LX-2 (ACTIVE) and CAF cells compared with the untreated control ($p < 0.01$), indicating a strong pro-proliferative effect (Figure 10D). These findings indicate that the integrity of ACTA2 signaling is required for the full pro-proliferative effect of TCDD in LX-2 (ACTIVE) and CAF cells. In other words, while TCDD alone increased stromal cell proliferation, this proliferative boost was largely abolished when ACTA2 was experimentally upregulated, underscoring a critical modulatory role for ACTA2 in TCDD-mediated cell growth.

We further probed the downstream signaling pathways involved. Given the strong enrichment of PI3K/Akt signaling observed in ACTA2-low tumors in our transcriptomic analyses, we measured the expression of key genes in the PI3K–AKT–mTOR pathway in LX-2 (ACTIVE) and CAF cells. Remarkably, TCDD treatment led to a significant upregulation of PIK3CA (encoding the p110α catalytic subunit of PI3K), AKT1, and MTOR transcripts (Figure 10E–G), indicating that TCDD exposure activates the PI3K–AKT–mTOR axis at the mRNA level, consistent with a pro-survival/pro-growth signaling response. In contrast, ACTA2 overexpression alone resulted in lower basal expression of these PI3K/Akt pathway genes, and, importantly, TCDD failed to induce their upregulation in ACTA2-overexpressing LX-2 (ACTIVE) and CAF cells. The mRNA levels of PIK3CA, AKT1, and MTOR in the TCDD + Ov-ACTA2 groups remained comparable to those in the Ov-ACTA2 alone groups (Figure 10E–G), suggesting that ACTA2 is necessary for TCDD-triggered activation of the PI3K/Akt pathway in these stromal cells.

Collectively, these in vitro results demonstrate that TCDD promotes the proliferation of LX-2 (ACTIVE) cells and CAFs by suppressing ACTA2 and consequently activating the PI3K/Akt signaling pathway, thereby driving the expression of key growth-regulatory genes. When ACTA2 is experimentally overexpressed, the proliferative and signaling effects of TCDD are abolished, highlighting ACTA2 as a critical mediator of TCDD's tumor-promoting actions in liver tumor–associated stromal cells.

To confirm the effect of ACTA2 on the PI3K-AKT-mTOR signaling pathway, both gain- and loss-of-function approaches were employed. ACTA2 overexpression lentivirus was transduced into LX-2 (ACTIVE) cells and CAF cells. Compared with the untransfected cells in the NC group, the ACTA2 protein level was significantly elevated (Figure 11A and B). Western Blot results showed that compared with the negative control (NC) group, the phosphorylation levels of key nodes in the PI3K-AKT-mTOR signaling pathway were significantly decreased in ACTA2-overexpressing cells, with markedly weakened protein band signals for p-PI3K, p-AKT, and p-mTOR, while the total levels of these proteins and the internal reference β-actin showed no significant changes (Figure 11C and D). This result indicates that ACTA2 overexpression can effectively inhibit the activation of the PI3K-AKT-mTOR signaling pathway.

To further validate the causal role of ACTA2, siRNA-mediated knockdown experiments were performed. As shown in Figure 11E and F, ACTA2 protein expression was significantly reduced in si-ACTA2-transfected LX-2 (ACTIVE) cells and CAFs compared with the NC group, confirming efficient knockdown. Notably, ACTA2 silencing led to a marked increase in the phosphorylation levels of PI3K, AKT, and mTOR, as evidenced by enhanced band intensity of p-PI3K, p-AKT, and p-mTOR, while total protein levels remained largely unchanged (Figure 11G and H). Quantitative densitometric analysis further confirmed that the ratios of phosphorylated to total proteins (p-PI3K/PI3K, p-AKT/AKT, and p-mTOR/mTOR) were significantly elevated following ACTA2 knockdown. The detailed mechanism is summarized in Figure 11I.

Together, these findings from both overexpression and knockdown experiments consistently demonstrate that ACTA2 negatively regulates PI3K–AKT–mTOR signaling, thereby supporting a causal role for ACTA2 in modulating this pathway.

Stromal-Derived Conditioned Media Enhances Clonogenic Growth of Hepatocellular Carcinoma Cells

To further investigate whether stromal-derived signals influence tumor cell behavior, colony formation assays were performed using conditioned media from LX-2 cells and CAFs.

As shown in Figure 12A and B, conditioned media derived from CAFs markedly increased the clonogenic capacity of both Huh7 and Hep3B cells compared with LX-2-derived conditioned media. Quantitative analysis demonstrated a significant increase in colony numbers in the CAF-CM group in both cell lines ($p < 0.01$).

These findings indicate that tumor-associated fibroblasts exert stronger pro-tumorigenic effects on hepatocellular carcinoma cells than LX-2 cells, likely through paracrine signaling mechanisms.

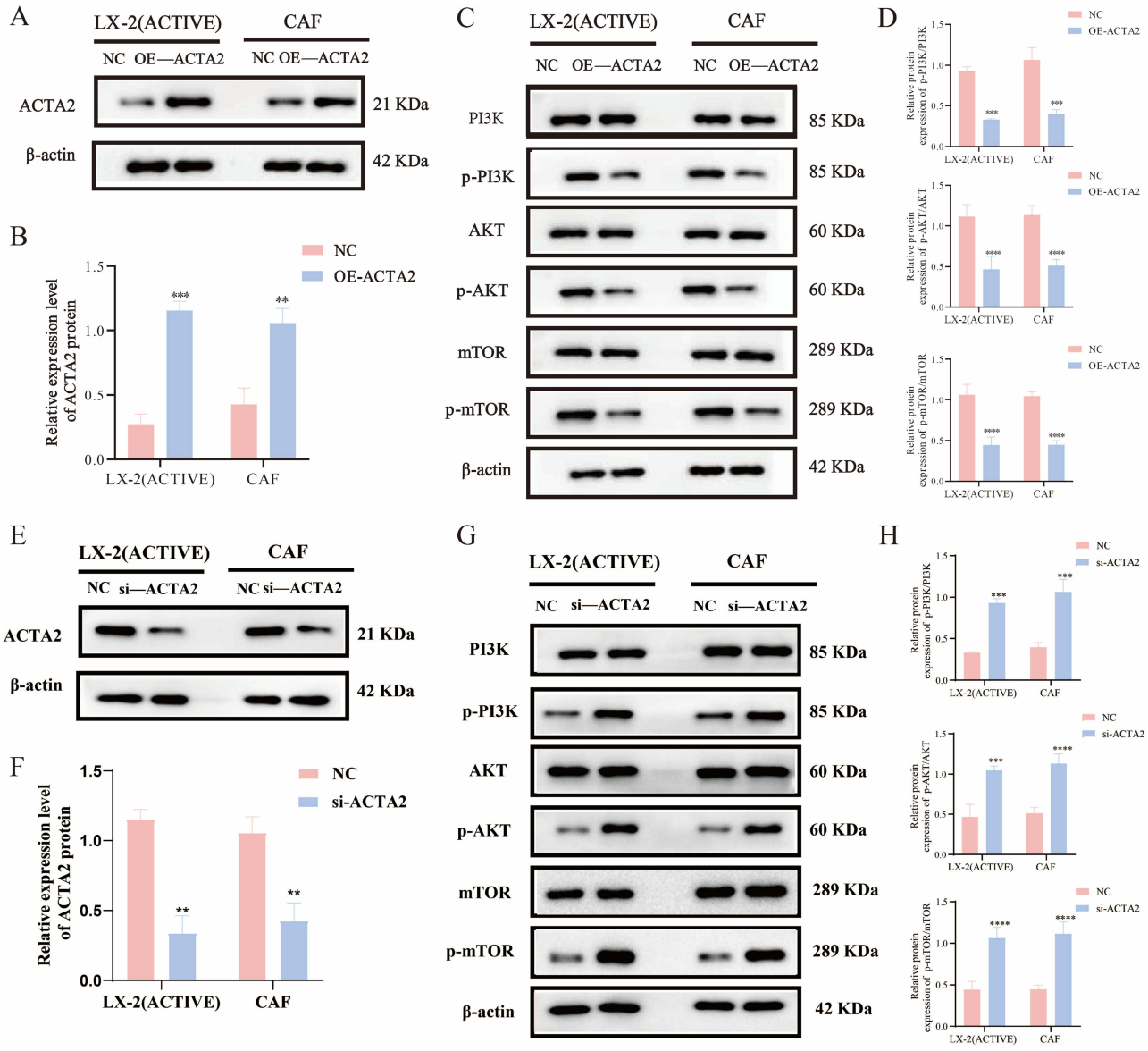

Figure 11 Continued.

https://doi.org/10.2147/JHC.S586916

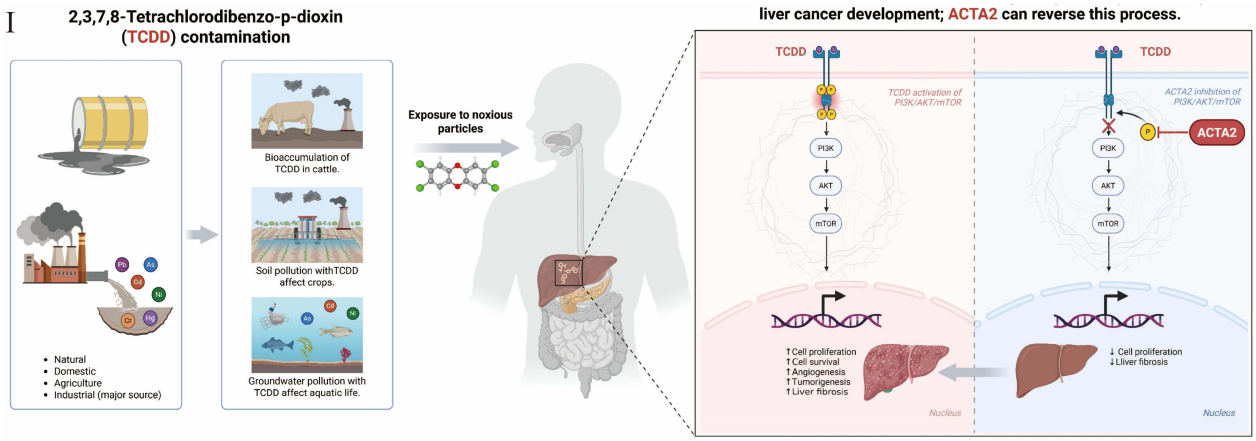

Figure 11 ACTA2 bidirectionally regulates the PI3K–AKT–mTOR signaling pathway in LX-2 (ACTIVE) cells and CAFs. (**A**) Representative Western blots showing ACTA2 and β-actin protein levels in LX-2 (ACTIVE) cells and CAFs transduced with negative control lentivirus (NC) or ACTA2-overexpressing lentivirus (OE-ACTA2). (**B**) Quantification of ACTA2 protein expression in LX-2 (ACTIVE) cells and CAFs. ACTA2 levels are markedly increased in the OE-ACTA2 groups compared with NC, confirming successful overexpression. (**C**) Representative Western blots of total and phosphorylated PI3K, AKT, and mTOR (PI3K/p-PI3K, AKT/p-AKT, mTOR/p-mTOR) and β-actin in LX-2 (ACTIVE) cells and CAFs following NC or OE-ACTA2 transduction. ACTA2 overexpression reduces the phosphorylation of PI3K, AKT, and mTOR without altering total protein levels. (**D**) Densitometric analysis of p-PI3K, p-AKT, and p-mTOR protein levels in LX-2 (ACTIVE) cells and CAFs, normalized to total protein and β-actin. Phosphorylation of all three proteins is significantly decreased in the OE-ACTA2 groups compared with NC, indicating inhibition of PI3K–AKT–mTOR pathway activation. (**E**) Representative Western blot images showing ACTA2 and β-actin protein levels in LX-2 (ACTIVE) cells and CAFs transfected with negative control siRNA (NC) or ACTA2-specific siRNA (si-ACTA2). (**F**) Quantification of ACTA2 protein expression in LX-2 (ACTIVE) cells and CAFs. ACTA2 levels are significantly decreased in the si-ACTA2 groups compared with NC, confirming efficient knockdown. (**G**) Representative Western blot images of PI3K, p-PI3K, AKT, p-AKT, mTOR, p-mTOR, and β-actin in LX-2 (ACTIVE) cells and CAFs following NC or si-ACTA2 transfection. ACTA2 knockdown increases the phosphorylation of PI3K, AKT, and mTOR without affecting total protein levels. (**H**) Densitometric analysis of p-PI3K, p-AKT, and p-mTOR normalized to total protein levels. The phosphorylation levels are significantly elevated in the si-ACTA2 groups compared with NC, indicating activation of the PI3K–AKT–mTOR signaling pathway. (**I**) Schematic illustration summarizing the proposed mechanism: environmental TCDD contamination leads to exposure and activation of the PI3K–AKT–mTOR signaling pathway, promoting liver cancer development, whereas ACTA2 overexpression counteracts this process by suppressing pathway activation and limiting tumor progression. Upward arrows (↑) represent increased or activated biological processes, whereas downward arrows (↓) indicate decreased or inhibited processes. TCDD and ACTA2 are highlighted in red to emphasize their roles as key regulatory factors in the proposed mechanism. Band intensities were quantified by densitometric analysis using ImageJ software. Data in panels (**B**) and (**D**) are presented as mean ± SEM from at least three independent experiments. $^{**}p < 0.01$, $^{***}p < 0.001$, $^{****}p < 0.0001$ versus NC.

Importantly, these results support the notion that ACTA2-associated stromal regulation does not primarily act through tumor cell–intrinsic expression, but rather through microenvironment-mediated interactions, thereby influencing tumor cell proliferation and survival.

Discussion

Our study reveals a mechanistic link between TCDD exposure and LIHC, centered on ACTA2 dysregulation and activation of the PI3K–AKT–mTOR pathway. As one of the most toxic dioxins, TCDD is recognized primarily as a tumor promoter that fosters a microenvironment conducive to malignant transformation. Consistent with this role, we observed that TCDD activated pro-survival signaling within the tumor microenvironment through the PI3K/Akt axis, a pathway known to suppress apoptosis and enhance proliferation. Previous studies have reported similar PI3K/Akt activation by TCDD in other tissues, and its inhibition attenuates TCDD-induced survival advantages. In our model, TCDD robustly increased downstream mTOR signaling, indicating that the PI3K–AKT–mTOR axis is a principal target of dioxin action in the liver. Given that this pathway is frequently dysregulated in LIHC, its activation by TCDD may mimic oncogenic signaling, lowering the threshold for hepatocyte transformation and promoting tumor progression. To enhance the robustness of our findings, multiple independent databases were integrated in this study. Although some analyses reveal consistent patterns, such as the stromal localization of ACTA2, this convergence across platforms strengthens the reliability of the observations rather than representing redundancy. Each dataset provides complementary information, including expression validation, cellular localization, immune associations, and mechanistic context. Together, these multi-dimensional analyses enable a more comprehensive understanding of ACTA2 in LIHC.

A key finding of this study is the identification of ACTA2 as a protective mediator in TCDD-exposed liver cells. Unlike classical oncogenic factors, overexpression of ACTA2 suppressed TCDD-induced activation of the PI3K, AKT, and mTOR pathways, indicating that ACTA2 may counterbalance pro-survival signaling in hepatocytes. This finding is

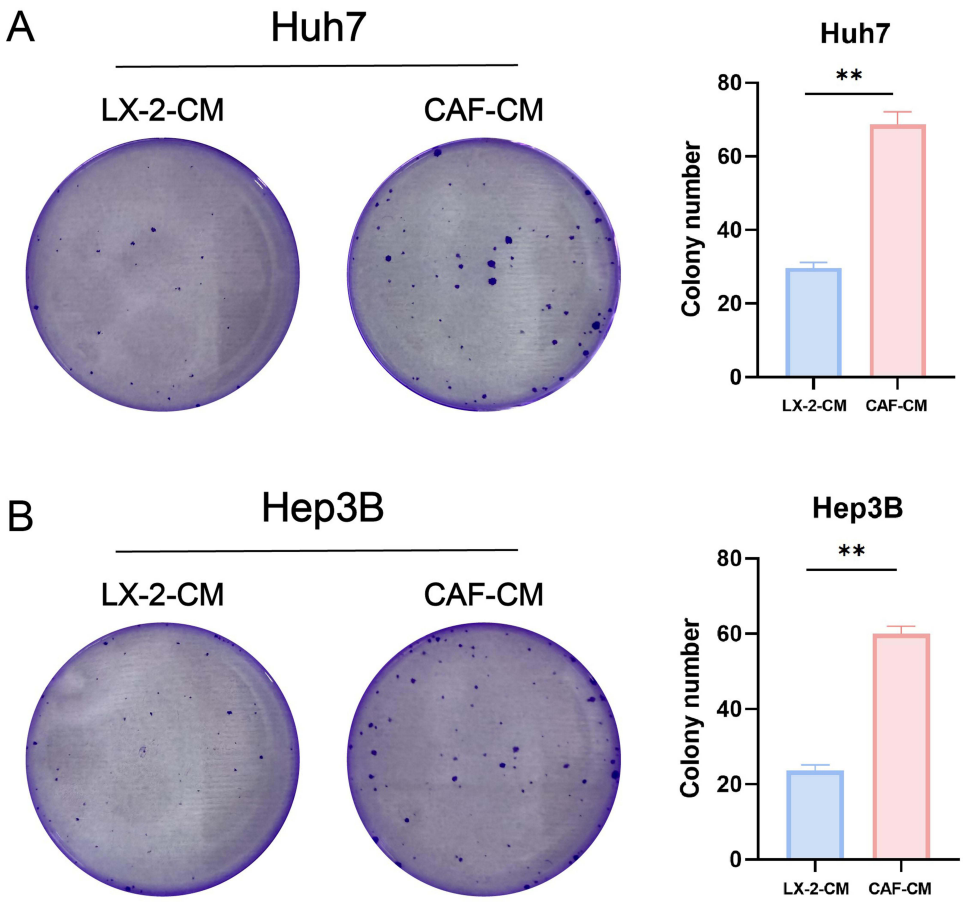

Figure 12 CAF-derived conditioned media promotes clonogenic growth of hepatocellular carcinoma cells. (**A**) Representative colony formation images of Huh7 cells cultured with conditioned media derived from LX-2 or cancer-associated fibroblasts (CAFs). (**B**) Representative colony formation images of Hep3B cells under the same conditions. Quantitative analysis showed that CAF-derived conditioned media significantly increased the number of colonies compared with LX-2-derived conditioned media in both cell lines. Data are presented as mean ± SD (n = 3). Statistical significance was determined using Student's *t*-test. **p < 0.01.

consistent with our bioinformatic analyses, which showed that higher ACTA2 expression correlates with longer overall survival in LIHC patients. Given that ACTA2 is predominantly expressed in hepatic stellate cells and myofibroblasts, its elevation likely reflects an active fibrotic response that limits malignant proliferation by maintaining stromal integrity. Therefore, ACTA2 may function as a context-dependent protective factor, restraining PI3K–AKT–mTOR signaling and moderating tumor-promoting inflammation in early-stage disease.

Importantly, the apparent classification of ACTA2 as a tumor suppressor requires careful interpretation. ACTA2 is a well-established marker of activated hepatic stellate cells and myofibroblasts and is not typically expressed in hepatocellular carcinoma cells themselves. Therefore, its expression in bulk tumor datasets largely reflects stromal composition rather than tumor cell–intrinsic activity. The observed upregulation of ACTA2 in HCC tissues, particularly in fibrosis-associated cases, is more likely indicative of increased stromal activation and fibrotic remodeling rather than a direct anti-proliferative function within tumor cells. This reconciles the apparent discrepancy between its low mutation frequency and low tumor cell expression and its association with improved clinical outcomes. Thus, ACTA2 should not be interpreted as a classical tumor suppressor gene, but rather as a context-dependent stromal regulator that exerts indirect effects on tumor progression through modulation of the tumor microenvironment.

Interestingly, bioinformatic survival analysis indicated that ACTA2 expression correlates with better overall survival in LIHC patients, suggesting a potential protective association. This apparent paradox can be rationalized by the fibrotic background and tumor purity differences among LIHC samples. Elevated ACTA2 in tumor tissues likely reflects concurrent liver fibrosis or cirrhosis, common in LIHC patients, rather than oncogenic ACTA2 expression within malignant hepatocytes.

https://doi.org/10.2147/JHC.S586916

Studies have shown that stromal gene signatures—particularly those derived from activated HSCs—can associate with improved prognosis when tumors retain substantial non-malignant parenchyma or organized perivascular α-SMA architecture (Wang et al, PLoS One, 2013). Conversely, as LIHC advances, tumor cell proportion increases and stromal fibroblast content declines, leading to lower ACTA2 expression and poorer outcomes. This pattern mirrors purity-dependent prognostic shifts observed in multiple LIHC datasets (Zhao et al, Front Oncol, 2023). Moreover, the functional heterogeneity of CAFs may underlie this duality: α-SMA$^+$ myofibroblastic CAFs can exert tumor-restraining effects by maintaining vascular integrity and limiting necrotic spread (Affo et al, J Hepatol, 2021). Therefore, high ACTA2 expression in bulk analyses may indicate a fibrosis-enriched yet less aggressive tumor microenvironment, whereas its loss reflects stromal depletion and progression toward a more malignant phenotype.

This work also demonstrates the value of network toxicology in elucidating environmental carcinogenesis. By integrating toxicogenomic and cancer datasets, ACTA2 was identified as an unexpected but central connector between TCDD exposure and oncogenic signaling. This systems-level approach highlights how environmental stressors reshape intracellular networks beyond direct genotoxic effects. Future toxicological evaluations should therefore account for indirect mechanisms—such as fibrosis-mediated and metabolic pathways—that sustain chronic disease and carcinogenesis.

From a translational perspective, the PI3K–AKT–mTOR axis represents a promising therapeutic target in toxin-related liver cancer. Pharmacological inhibitors of this pathway are already in clinical development for LIHC and could potentially mitigate TCDD-driven tumor promotion. Targeting the fibrotic microenvironment may also yield benefit, as ACTA2$^+$ myofibroblasts and CAFs sustain paracrine signaling that fuels tumor progression. Anti-fibrotic or stroma-modulating therapies, alongside preventive measures to reduce dioxin exposure, could thus form an integrated strategy against environmental liver carcinogenesis.

Although the direct molecular link between ACTA2 and sorafenib resistance has not yet been fully elucidated, several plausible mechanisms may explain this association. ACTA2 encodes α-smooth muscle actin (α-SMA), a canonical marker of activated myofibroblasts and CAFs, and therefore may reflect a stromal state that favors therapeutic resistance rather than acting solely as a cell-autonomous resistance factor.[51] In HCC, CAFs have been reported to promote sorafenib resistance through paracrine signaling pathways such as HGF/MET/ERK and CXCL12/CXCR4.[52]

Despite these findings, several limitations of the present study should be acknowledged. First, our experimental validation was primarily conducted using in vitro cell models, including LX-2 cells and cancer-associated fibroblasts, which may not fully recapitulate the complex cellular interactions and spatial heterogeneity of the in vivo liver microenvironment. In particular, the absence of in vivo models limits our ability to assess the dynamic interplay between stromal cells, immune components, and hepatocytes during TCDD-induced hepatocarcinogenesis. Future studies employing animal models or spatial transcriptomic approaches will be essential to validate the stromal–tumor interactions proposed in this study. Second, our analyses rely heavily on integrative bioinformatic approaches using public datasets. Although cross-platform validation enhances robustness, bulk transcriptomic data inherently reflect mixed cell populations and may be influenced by tumor purity and stromal composition. While we have addressed this issue by incorporating single-cell analyses and emphasizing the stromal origin of ACTA2, further experimental validation at the tissue level, such as immunohistochemistry or spatial profiling, would strengthen the biological interpretation. Finally, while our results suggest that ACTA2 modulates PI3K–AKT–mTOR signaling in a stromal-dependent manner, the precise molecular mechanisms underlying this regulation remain to be fully elucidated. It is possible that ACTA2 influences tumor progression indirectly through extracellular matrix remodeling, paracrine signaling, or mechanotransduction pathways. Further mechanistic studies are required to dissect these interactions and to determine whether ACTA2 directly or indirectly regulates oncogenic signaling cascades in hepatocellular carcinoma.

In conclusion, TCDD promotes hepatocarcinogenesis through ACTA2-dependent activation of the PI3K–AKT–mTOR signaling network. This mechanism links fibrogenic activation with metabolic and proliferative reprogramming in hepatocytes. By inducing ACTA2 expression while activating the PI3K–AKT–mTOR axis, TCDD fosters a microenvironment that supports sustained growth, survival, and metabolic adaptation—hallmarks of malignant transformation. These findings deepen our understanding of how persistent pollutants drive liver cancer and emphasize the dual role of ACTA2: a fibrosis marker elevated in early disease yet a protective indicator of stromal integrity that diminishes with tumor progression. The ACTA2–PI3K–AKT–mTOR axis thus represents both a mechanistic hallmark and a promising target for therapeutic intervention.

In addition, we acknowledge that patient-level stratification based on fibrosis stage, tumor purity, or stromal proportion was not performed in the current study. Given the stromal-specific nature of ACTA2, these factors may influence its apparent expression patterns in bulk datasets. Importantly, however, multiple lines of evidence in our study consistently support the interpretation that ACTA2 primarily reflects stromal composition rather than tumor cell–intrinsic expression. These include (i) single-cell RNA-seq analyses demonstrating its predominant expression in hepatic stellate cells and fibroblast populations, and (ii) immune infiltration analyses in TIMER3.0 in which partial correlation was performed while controlling for tumor purity. Therefore, while the lack of explicit patient-level stratification represents a limitation, it is unlikely to fundamentally alter the central conclusion that ACTA2 functions as a stromal-context–dependent marker in hepatocellular carcinoma. Future studies incorporating spatial transcriptomics, deconvolution methods, or clinically annotated fibrosis staging data will further refine these observations.

Ethics Statement

This study involved the analysis of human-derived data obtained from publicly available databases, including TCGA and GEO. All original data were collected by the respective database providers with prior ethical approval and informed consent from participants.

The present study constitutes a secondary analysis of de-identified data and does not involve direct human subject participation. Therefore, according to the Measures for Ethical Review of Life Science and Medical Research Involving Human Subjects (National Health Commission of the People's Republic of China, issued February 18, 2023), studies using publicly available and anonymized data are exempt from ethical review (Article 32, Items 1 and 2).

In addition, the LX-2 cell line and the Cancer-Associated Fibroblasts (CAFs, LIHC) used in this study were commercially purchased from certified cell repositories. No human participants, personal data, or patient-derived primary tissues were involved. Therefore, this research does not require ethics approval and does not involve any ethical concerns.

Funding

This research was supported by the China National University Student Innovation & Entrepreneurship Development Program (No.202410422082) and Youth Student Basic Research Project, Shandong University (SDUQM2551).

Disclosure

The author(s) report(s) no conflicts of interest in this work.

References

1. Dong L, Tang NJ. Liver toxicity of 2,3,7,8-tetrachlorodibenzo-p-dioxin. *Zhonghua Lao dong Wei Sheng Zhi Ye Bing Za Zhi*. 2005;23(1):60–62.
2. Huff JE, Salmon AG, Hooper NK, Zeise L. Long-term carcinogenesis studies on 2,3,7,8-tetrachlorodibenzo-p-dioxin and hexachlorodibenzo-p-dioxins. *Cell Biol Toxicol*. 1991;7(1):67–94. doi:10.1007/bf00121331
3. Poland A, Kende A. 2,3,7,8-Tetrachlorodibenzo-p-dioxin: environmental contaminant and molecular probe. *Federation Proceed*. 1976;35(12):2404–2411.
4. Sorg O, Zennegg M, Schmid P, et al. 2,3,7,8-tetrachlorodibenzo-p-dioxin (TCDD) poisoning in Victor Yushchenko: identification and measurement of TCDD metabolites. *Lancet*. 2009;374(9696):1179–1185. doi:10.1016/s0140-6736(09)60912-0
5. Shoaf CR. 2,3,7,8-Tetrachlorodibenzo-p-dioxin toxicity mechanisms. *Toxicol Lett*. 1988;42(1):1–3. doi:10.1016/0378-4274(88)90096-3
6. Greenlee WF, Skopek TR, Gaido K, Walker C. Comparative genetic mechanisms of 2,3,7,8-tetrachlorodibenzo-p-dioxin (TCDD)-induced tumors. *Progr Clin Biol Res*. 1990;331:177–186.
7. Umbreit TH, Gallo MA. Physiological implications of estrogen receptor modulation by 2,3,7,8-tetrachlorodibenzo-p-dioxin. *Toxicol Lett*. 1988;42(1):5–14. doi:10.1016/0378-4274(88)90097-5
8. Dong Y, Wang WP, Lee WJ, et al. Hepatocellular carcinoma in the non-cirrhotic liver. *Clin Hemorheol Microcircul*. 2022;80(4):423–436. doi:10.3233/ch-211309
9. Tovoli F, Ferri S, Piscaglia F. Hepatocellular carcinoma in non alcoholic fatty liver disease. *Current Pharmaceut Design*. 2020;26(32):3909–3914. doi:10.2174/1381612826666200429093648
10. Ganesan P, Kulik LM. Hepatocellular carcinoma: new developments. *Clin Liver Dis*. 2023;27(1):85–102. doi:10.1016/j.cld.2022.08.004
11. Patrizi B, Siciliani de Cumis M. TCDD toxicity mediated by epigenetic mechanisms. *Int J Mol Sci*. 2018;19(12). doi:10.3390/ijms19124101
12. Gogal RM Jr, Holladay SD. Perinatal TCDD exposure and the adult onset of autoimmune disease. *J Immunotoxicol*. 2008;5(4):413–418. doi:10.1080/10408360802483201
13. Sensi B, Angelico R, Toti L, et al. Mechanism, potential, and concerns of immunotherapy for hepatocellular carcinoma and liver transplantation. *Current Mol Pharmacol*. 2024;17:e18761429310703. doi:10.2174/0118761429310703240823045808
14. Ye W, Wang J, Zheng J, Jiang M, Zhou Y, Wu Z. Association between higher expression of Vav1 in hepatocellular carcinoma and unfavourable clinicopathological features and prognosis. *Protein Peptide Lett*. 2024;31(9):706–713. doi:10.2174/0109298665330781240830042601

15. Peng Y, Wang Y, Zhou C, Mei W, Zeng C. PI3K/Akt/mTOR pathway and its role in cancer therapeutics: are we making headway? *Front Oncol*. 2022;12:819128. doi:10.3389/fonc.2022.819128
16. Ersahin T, Tuncbag N, Cetin-Atalay R. The PI3K/AKT/mTOR interactive pathway. *Mol Biosyst*. 2015;11(7):1946–1954. doi:10.1039/c5mb00101c
17. Kerkvliet NI. Recent advances in understanding the mechanisms of TCDD immunotoxicity. *Int Immunopharmacol*. 2002;2(2–3):277–291. doi:10.1016/s1567-5769(01)00179-5
18. Mu R, Chang M, Feng C, et al. Analysis of the expression of PRDX6 in patients with hepatocellular carcinoma and its effect on the phenotype of hepatocellular carcinoma cells. *Current Genom*. 2024;25(1):2–11. doi:10.2174/0113892029273682240111052317
19. He X, Ma J, Yan X, et al. CDT1 is a potential therapeutic target for the progression of NAFLD to HCC and the exacerbation of cancer. *Current Genom*. 2025;26(3):225–243. doi:10.2174/0113892029313473240919105819
20. Friedman SL. Hepatic stellate cells: protean, multifunctional, and enigmatic cells of the liver. *Physiolog Rev*. 2008;88(1):125–172. doi:10.1152/physrev.00013.2007
21. Kobayashi H, Gieniec KA, Lannagan TRM, et al. The origin and contribution of cancer-associated fibroblasts in colorectal carcinogenesis. *Gastroenterology*. 2022;162(3):890–906. doi:10.1053/j.gastro.2021.11.037
22. Kisseleva T, Brenner DA. Hepatic stellate cells and the reversal of fibrosis. *J Gastroenterol Hepatol*. 2006;21 Suppl 3:S84–S87. doi:10.1111/j.1440-1746.2006.04584.x
23. Kalluri R. The biology and function of fibroblasts in cancer. *Nat Rev Cancer*. 2016;16(9):582–598. doi:10.1038/nrc.2016.73
24. Hernandez-Gea V, Friedman SL. Pathogenesis of liver fibrosis. *Annual Rev Pathol*. 2011;6:425–456. doi:10.1146/annurev-pathol-011110-130246
25. Španko M, Pfeiferová L, Krejčí ED, et al. Gamma smooth muscle actin as a new potential marker of cancer-associated fibroblasts. *Histochem Cell Biol*. 2025;163(1):93. doi:10.1007/s00418-025-02419-9
26. Szklarczyk D, Santos A, von Mering C, Jensen LJ, Bork P, Kuhn M. STITCH 5: augmenting protein-chemical interaction networks with tissue and affinity data. *Nucleic Acids Res*. 2016;44(D1):D380–4. doi:10.1093/nar/gkv1277
27. Kuhn M, Szklarczyk D, Pletscher-Frankild S, et al. STITCH 4: integration of protein-chemical interactions with user data. *Nucleic Acids Res*. 2014;42(Database issue):D401–7. doi:10.1093/nar/gkt1207
28. Zdrazil B, Felix E, Hunter F, et al. The ChEMBL database in 2023: a drug discovery platform spanning multiple bioactivity data types and time periods. *Nucleic Acids Res*. 2024;52(D1):D1180–d92. doi:10.1093/nar/gkad1004
29. Uhlén M, Fagerberg L, Hallström BM, et al. Proteomics. Tissue-based map of the human proteome. *Science*. 2015;347(6220):1260419. doi:10.1126/science.1260419
30. Thul PJ, Åkesson L, Wiking M, et al. A subcellular map of the human proteome. *Science*. 2017;356(6340). doi:10.1126/science.aal3321
31. Sjöstedt E, Zhong W, Fagerberg L, et al. An atlas of the protein-coding genes in the human, pig, and mouse brain. *Science*. 2020;367(6482). doi:10.1126/science.aay5947
32. Karlsson M, Zhang C, Méar L, et al. A single-cell type transcriptomics map of human tissues. *Sci Adv*. 2021;7(31). doi:10.1126/sciadv.abh2169
33. Uhlen M, Zhang C, Lee S, et al. A pathology atlas of the human cancer transcriptome. *Science*. 2017;357(6352). doi:10.1126/science.aan2507
34. Uhlen M, Karlsson MJ, Zhong W, et al. A genome-wide transcriptomic analysis of protein-coding genes in human blood cells. *Science*. 2019;366(6472). doi:10.1126/science.aax9198
35. Uhlén M, Karlsson MJ, Hober A, et al. The human secretome. *Sci Signal*. 2019;12(609). doi:10.1126/scisignal.aaz0274
36. Vijay J, Gauthier MF, Biswell RL, et al. Single-cell analysis of human adipose tissue identifies depot and disease specific cell types. *Nat Metabol*. 2020;2(1):97–109. doi:10.1038/s42255-019-0152-6
37. Li M, Zhang X, Ang KS, et al. DISCO: a database of deeply integrated human single-cell omics data. *Nucleic Acids Res*. 2022;50(D1):D596–d602. doi:10.1093/nar/gkab1020
38. Li T, Fu J, Zeng Z, et al. TIMER2.0 for analysis of tumor-infiltrating immune cells. *Nucleic Acids Res*. 2020;48(W1):W509–w14. doi:10.1093/nar/gkaa407
39. Liu Z, Liu L, Weng S, et al. BEST: a web application for comprehensive biomarker exploration on large-scale data in solid tumors. *J Big Data*. 2023;10(1):165. doi:10.1186/s40537-023-00844-y
40. Liu Z, Yuan Z, Guo Y, et al. SMARTdb: An integrated database for exploring single-cell multi-omics data of reproductive medicine. *Genom Proteomics Bioinform*. 2024;22(3). doi:10.1093/gpbjnl/qzae005
41. Győrffy B. Integrated analysis of public datasets for the discovery and validation of survival-associated genes in solid tumors. *Innovation*. 2024;5(3):100625. doi:10.1016/j.xinn.2024.100625
42. Győrffy B. Transcriptome-level discovery of survival-associated biomarkers and therapy targets in non-small-cell lung cancer. *Brit J Pharmacol*. 2024;181(3):362–374. doi:10.1111/bph.16257
43. Cerami E, Gao J, Dogrusoz U, et al. The cBio cancer genomics portal: an open platform for exploring multidimensional cancer genomics data. *Cancer Discovery*. 2012;2(5):401–404. doi:10.1158/2159-8290.Cd-12-0095
44. Gao J, Aksoy BA, Dogrusoz U, et al. Integrative analysis of complex cancer genomics and clinical profiles using the cBioPortal. *Sci Signal*. 2013;6(269):pl1. doi:10.1126/scisignal.2004088
45. de Bruijn I, Kundra R, Mastrogiacomo B, et al. Analysis and visualization of longitudinal genomic and clinical data from the AACR project GENIE biopharma collaborative in cBioPortal. *Cancer Res*. 2023;83(23):3861–3867. doi:10.1158/0008-5472.Can-23-0816
46. Bateman A, Martin MJ, Orchard S, et al. UniProt: the universal protein knowledgebase in 2025. *Nucleic Acids Res*. 2025;53(D1):D609–d17. doi:10.1093/nar/gkae1010
47. Abramson J, Adler J, Dunger J, et al. Accurate structure prediction of biomolecular interactions with AlphaFold 3. *Nature*. 2024;630(8016):493–500. doi:10.1038/s41586-024-07487-w
48. Sun D, Wang J, Han Y, et al. TISCH: a comprehensive web resource enabling interactive single-cell transcriptome visualization of tumor microenvironment. *Nucleic Acids Res*. 2021;49(D1):D1420–d30. doi:10.1093/nar/gkaa1020
49. Han Y, Wang Y, Dong X, et al. TISCH2: expanded datasets and new tools for single-cell transcriptome analyses of the tumor microenvironment. *Nucleic Acids Res*. 2023;51(D1):D1425–d31. doi:10.1093/nar/gkac959
50. Jackson E, Shoemaker R, Larian N, Cassis L. Adipose tissue as a site of toxin accumulation. *Comprehensive Physiol*. 2017;7(4):1085–1135. doi:10.1002/cphy.c160038

51. Peng H, Zhu E, Zhang Y. Advances of cancer-associated fibroblasts in liver cancer. *Bio Marker Res*. 2022;10(1):59. doi:10.1186/s40364-022-00406-z
52. Zhao J, Lin E, Bai Z, et al. Cancer-associated fibroblasts induce sorafenib resistance of hepatocellular carcinoma cells through CXCL12/FOLR1. *BMC Cancer*. 2023;23(1):1198. doi:10.1186/s12885-023-11613-8